Edge states and the Periodic Self-Sustaining Process in the Stokes boundary layer

J. Sandoval[1]† and T.S. Eaves[1]

[1]School of Science and Engineering, University of Dundee, Dundee DD1 4HN, UK

(Received xx; revised xx; accepted xx)

Abstract: The Stokes boundary layer (SBL) is the oscillating flow above a flat plate. Its laminar flow becomes linearly unstable at a Reynolds number of $Re = U_0\sqrt{T_0/\nu} \approx 2511$, where U_0 is the amplitude of the oscillation, T_0 is the period of oscillation, and ν is the fluid's kinematic viscosity, but turbulence is observed subcritically for $Re \gtrsim 700$. The state space consists of laminar and turbulent basins of attraction, separated by a saddle point (the 'edge state') and its stable manifold (the 'edge'). This work presents the edge trajectories for the transitional regime of the SBL. Despite linear dynamics disallowing the lift-up mechanism in the laminar SBL, edge trajectories are dominated by coherent structures as in other canonical shear flows: streaks, rolls, and waves. SBL structures are inherently periodic, interacting with the oscillating flow in a novel way: streaks form near the plate, migrate upward at a speed $2\sqrt{\pi}$, and dissipate. A streak-roll-wave decomposition reveals a spatio-temporally evolving version of the Self-Sustaining Process (SSP): (i) rolls lift fluid near the plate, generating streaks (via the lift-up mechanism), (ii) streaks can only persist in regions with the same sign of laminar shear as when they were created, defining regions that moves upward at a speed $2\sqrt{\pi}$, (iii) the sign of streak production reverses at a roll stagnation point, destroying the streak and generating waves, (iv) trapped waves reinforce the rolls via Reynolds stresses, (v) mass conservation reinforces the rolls. This Periodic SSP highlights the role of flow oscillations in sustaining transitional structures in the SBL, providing an alternative picture to 'bypass' transition, which relies on pre-existing free stream turbulence and spanwise vortices.

Key words:

1. Introduction

Oscillatory flows are ubiquitous in nature (Jensen *et al.* 1989; Spalart & Baldwin 1987), biomechanical systems (Ku 1997; Taylor & Draney 2004) and engineering applications (Adcock *et al.* 2021; Gatti & Quadrio 2016), with ongoing research including a particular focus on transition to turbulence in oscillatory boundary layers (Blennerhassett & Bassom 2008; Biau 2016; Xiong *et al.* 2020; Blondeaux *et al.* 2021; Gong *et al.* 2022). The canonical oscillating flow is the Stokes Boundary Layer (SBL), the flow above a sinusoidally oscillating

† Email address for correspondence: jsandoval001@dundee.ac.uk

flat plate. The transition to turbulence in this flow is complex (von Kerczek & Davis 1974; Blennerhassett & Bassom 2008; Mujal-Colilles *et al.* 2016; Blondeaux & Vittori 2021); the SBL is a subcritical flow that exhibits turbulent dynamics at Reynolds numbers $Re = U_0\sqrt{T_0/\nu}$ (where U_0 is the velocity oscillation amplitude, T_0 is the oscillation period, and ν is the fluid's kinematic viscosity) below the critical Reynolds number $Re_c \approx 2511$ at which the laminar solution becomes linearly unstable to normal mode perturbations (Blennerhassett & Bassom 2002), although convective linear instability occurs below this critical value in domains with a large horizontal extent (Ramage *et al.* 2020; Pretty *et al.* 2021). The critical Reynolds number found by Blennerhassett & Bassom (2002) is based upon a Floquet analysis of perturbations growing over the whole oscillation cycle.

Ozdemir *et al.* (2014) summarised several theoretical, experimental and numerical works on the SBL and categorised the flow into four regimes: (i) Laminar ($Re < Re_{c_1}$), (ii) Disturbed Laminar ($Re_{c_1} < Re < Re_{c_2}$), where some disturbances such as spanwise vortices are observed, but without enough growth to trigger transition, (iii) Intermittently Turbulent ($Re_{c_2} < Re < Re_{c_3}$), where some turbulent features such as bursts of energy during the mid and late deceleration phases are observed, which laminarise during the early acceleration phase, and (iv) Turbulent ($Re > Re_{c3}$). Around the onset of the intermittently turbulent regime, Ozdemir *et al.* (2014) observed a self-sustaining transitional behaviour, and this has been described in terms of a 'bypass' transition in which streamwise streaks triggered by free stream turbulence grow, form hairpin vortices, and then eject a spanwise vortex back into the free stream, which subsequently breaks down to turbulence and reinitiates the cycle (Xiong *et al.* 2020; Gong *et al.* 2022). Mier *et al.* (2021) and Fytanidis *et al.* (2021) reported that this self-sustaining transitional behaviour is associated with a phase-lag between the wall-shear stress and the laminar velocity, with disturbances growing during the deceleration phase and decaying during the acceleration phase (see also Luo & Wu 2010), an observation in agreement with the transitional cycles observed in other, wall-bounded oscillating flows (Pier & Schmid 2017; Ebadi *et al.* 2019; Pier & Schmid 2021; Linot *et al.* 2024).

Crucially, however, such a 'self-sustaining' bypass transition relies upon turbulent motions and strong spanwise vortices. This sets it apart from the coherent motions of the Vortex-Wave Interaction states (Hall & Smith 1991; Hall & Sherwin 2010), often realised as 'edge states' controlling the transition to turbulence in steady wall–bounded shear flows (Skufca *et al.* 2006; Kim & Moehlis 2008; Schneider & Eckhardt 2006; Duguet *et al.* 2009; Schneider *et al.* 2010; Eaves & Caulfield 2015) which follow the Self-Sustaining Process (SSP) (Waleffe 1997) of streamwise vortices created via the lift-up mechanism (Landahl 1980) and sustained by weak three-dimensional waves. From a dynamical systems point of view, laminar and turbulent flows can be seen as attractors in a high-dimensional state-space, whose basins of attraction are separated by a manifold termed the 'edge of chaos' (or simply the 'edge') (Skufca *et al.* 2006), containing local attractors known as 'edge states'. Characterisation of these edge states offers an alternative view of the physics associated with transition to turbulence which is self-contained, omitting the need to invoke pre-existing free stream turbulence to initiate transition, and, in the case of steady shear flows, requiring only streamwise vortices. Furthermore, the mechanisms underlying such states are also known to control important processes in the fully turbulent flow (see e.g. Kawahara *et al.* 2012; Budanur *et al.* 2017).

In steady wall-bounded shear flows, these edge states rely on the lift-up mechanism, a linear transient growth mechanism by which parcels of fluid are advected ('lifted') through a shear flow, for example taking high-speed fluid and moving it to a low-speed region, creating streamwise momentum defects. Continued advection leads to large transient growth over a long ($\mathcal{O}(Re)$) timescale, and is responsible for producing large-amplitude ($\mathcal{O}(1)$)

streamwise streaks when realised at finite amplitude. A steady background shear allows the lift-up mechanism to accumulate momentum defects in fixed locations over a long period of time, and so it is often the linear mechanism with the largest, and longest sustained, growth (Butler & Farrell 1992) and hence is integral to the SSP (Waleffe 1997). However, in the SBL, the lift-up mechanism is not an optimal linear transient growth mechanism (Biau 2016) since the laminar shear flow is periodically oscillating, preventing momentum defects from accumulating in a single location, and reversing sign every half-period. Instead, the Orr mechanism (Orr 1907) is dominant, which allows for moderate growth as spanwise vortices are tilted by the background shear over a short timescale. It is known that even small disruptions to the lift-up mechanism have the potential to significantly affect edge state dynamics (Eaves & Caulfield 2015).

These observations raise the interesting question as to what self-sustaining mechanism(s) edge states in the SBL utilise to balance dissipation (relaminarisation) against instability (transition to turbulence). On the one hand, a traditional interpretation of the SSP as using the lift-up mechanism due to its optimal linear growth would potentially point to new, Orr-based edge states for the SBL. On the other hand, transitional SBL flows are observed to consist of streamwise streaks (Sarpkaya 1993; Costamagna *et al.* 2003) and so perhaps some nonlinearity associated with the edge state dynamics allows the lift-up mechanism enough 'time' to create large-amplitude streaks. The most well-studied edge states have been steady, and so the different components of the SSP act all together at the same time, however in this second, lift-up based scenario, any realisation of the SSP in the SBL would evolve periodically in order to accommodate the alternating shear direction of the background flow, opening up the potential for components of the SSP to act sequentially. In order to make some connection with the bypass transition scenario, whatever mechanisms arise within the edge state dynamics should shed light upon how boundary layer ejections could be initiated without resorting to pre-existing turbulence.

In this work, we compute edge trajectories in the transitional regime of the SBL and analyse their dynamics in order to determine the underlying physical mechanisms which sustain them. We demonstrate that the edge states are periodically evolving versions of the SSP, utilising the lift-up mechanism, and that a temporal interplay between the laminar shear and streak nonlinearity results in streak migration away from the wall (non-turbulent ejections) and sequential activation of different components of the flow. In §2 we present the equations of motion, the numerical model, and the edge tracking algorithm. In §3 we provide an overview of the edge trajectory dynamics, which are examined in closer detail in section §4 which presents a complete analysis of the Periodic Self-Sustaining Process (PSSP). Conclusions are drawn in §5.

2. Methodology

2.1. *Equations of motion*

The Stokes boundary layer is the oscillatory flow above a flat plate, in which an oscillation of period T_0 is driven either by a sinusoidal oscillation in the velocity of the plate itself (in the x-direction) of magnitude U_0 or a sinusoidal oscillation of the pressure gradient above a stationary plate; in this work, we study the former, oscillating plate flow. These oscillations set up a boundary layer against the plate whose thickness is determined diffusively, leading to the characteristic length-scale $\delta = \sqrt{\nu T_0}$ in which ν is the kinematic viscosity of the fluid. We decompose the instantaneous velocity into the sum of a laminar component $\boldsymbol{U} = (U, 0, 0)$ and a perturbation velocity field $\boldsymbol{u} = (u, v, w)$, such that $\boldsymbol{u}^{tot} = \boldsymbol{U} + \boldsymbol{u}$. Using index notation,

the dimensionless incompressible Navier–Stokes equations for this flow read

$$\frac{\partial u_i}{\partial x_i} = 0, \tag{2.1}$$

$$\frac{\partial u_i}{\partial t} + Re\left[U_j\frac{\partial u_i}{\partial x_j} + u_j\frac{\partial U_i}{\partial x_j} + u_j\frac{\partial u_i}{\partial x_j}\right] = -\frac{\partial p}{\partial x_i} + \frac{\partial^2 u_i}{\partial x_j \partial x_j}, \tag{2.2}$$

where the Reynolds number is given by

$$Re = \frac{U_0\sqrt{\nu T_0}}{\nu} = U_0\sqrt{\frac{T_0}{\nu}}, \tag{2.3}$$

which follows the definition adopted by Biau (2016). We note that this definition of the Reynolds number is a factor of $\sqrt{\pi}$ larger than that of von Kerczek & Davis (1974); Ozdemir *et al.* (2014) and others, and is a factor of $2\sqrt{\pi}$ larger than that of Blennerhassett & Bassom (2002); Ramage *et al.* (2020) and others; all values quoted here, including the critical linear stability threshold $Re_c \approx 2511$ have been converted to match (2.3). The boundary conditions are

$$u_i^{tot} = \delta_{1i}U(0,t) \quad \text{at} \quad y = 0, \tag{2.4}$$

$$u_i^{tot} \to 0 \quad \text{as} \quad y \to \infty, \tag{2.5}$$

where δ_{ij} is the Kronecker delta.

The laminar flow $\boldsymbol{U} = (U(y,t), 0, 0)$ is directed along the x-axis and varies in the vertical y-direction. The laminar flow is the well-known solution to the Stokes second problem, and is given by

$$U(y,t) = \cos(2\pi t - \sqrt{\pi}y)e^{-\sqrt{\pi}y}, \tag{2.6}$$

The laminar flow is periodic with period $T = 1$, and it has a (time-)shift-reflect symmetry

$$U(y, t + T/2) = -U(y,t). \tag{2.7}$$

Local features of the laminar flow (such as maxima, minima, inflection points, etc.) move upward away from the wall at a constant speed of $2\sqrt{\pi}$.

With this laminar flow, the boundary conditions for the perturbation velocity are

$$u_i = 0 \quad \text{at} \quad y = 0, \tag{2.8}$$

$$u_i \to 0 \quad \text{as} \quad y \to \infty. \tag{2.9}$$

However, for numerical purposes a bounded domain is used, in which the streamwise x and spanwise z directions are periodic, and a large wall-normal extent L_y is chosen, at which impenetrable and stress-free boundary conditions are applied,

$$v = 0 \quad \text{and} \quad \frac{\partial u}{\partial y} = \frac{\partial w}{\partial y} = 0 \quad \text{at} \quad y = L_y. \tag{2.10}$$

A schematic representation of the oscillating wall problem is presented in figure 1.

2.2. *Numerical implementation and setup*

We solve equations (2.1–2.2) for the perturbation velocity u_i with boundary conditions (2.8) and (2.10) using the DNS solver Diablo (Taylor 2008). This code employs pseudo-spectral methods to compute spatial derivatives and uses a third-order Runge–Kutta scheme for time integration, and a 2/3 de-aliasing rule is applied to deal with the nonlinear terms. The simulations are carried out in parallel using the MPI library.

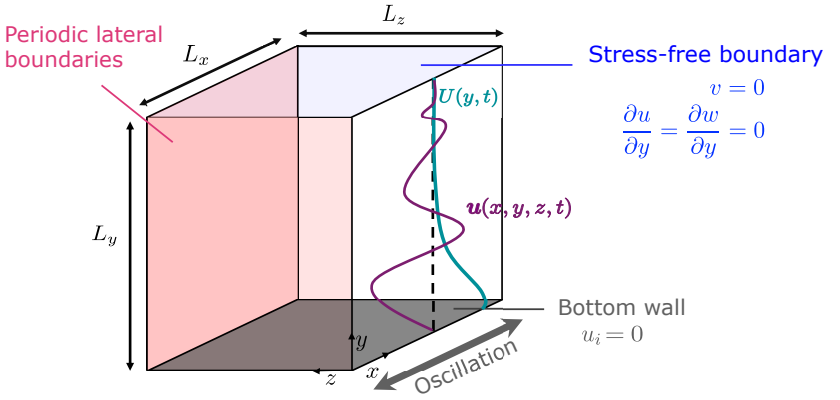

Figure 1: Problem diagram for flow above an oscillating wall. The lateral boundaries (x and z) are periodic. In the wall-normal direction, the perturbation velocity satisfies the no-slip condition, while the upper boundary is impenetrable and stress free.

The equations are solved in a rectangular domain of size $L_x = L_z = 8.2$ and $L_y = 10.0$. The size of L_x (and also L_z) is chosen to match the wavenumber of the largest transiently growing linear disturbance at $Re = 1000$ (Biau 2016). The periodic x and z directions are discretised using a uniform grid with $N_x = 64$ and $N_z = 32$ Fourier modes, respectively. Initial tests used the same resolution as Biau (2016), $N_x = N_z = 128$, but this was scaled back for efficiency since turbulent scales do not need to be resolved in order to accurately compute the much simpler edge trajectories, and there was no significant loss in accuracy found when doing so. The y direction is discretised using $N_y = 241$ grid points, which are stretched away from the wall to ensure an efficient and accurate representation of the structures near the wall. The results are insensitive to other values of N_y around this choice. A narrower geometry with $L_z = 4.1$ and $N_z = 16$ is also briefly considered, and the resulting dynamics are discussed in the next section.

2.3. *Edge Tracking*

Trajectories along the edge manifold may be found by 'edge tracking' (Skufca *et al.* 2006; Toh & Itano 2003; Schneider *et al.* 2007; Kreilos *et al.* 2013), an iterative procedure in which trajectories of initial conditions either side of the edge are computed and bisected depending on how they evolve in time. To classify trajectories as leading to laminar or turbulent flow, we use the L_2-norm of the perturbation velocity field as a proxy ($E = 0$ is the laminar state by construction):

$$E(\boldsymbol{u}) = \frac{1}{V_\Omega} \int_\Omega \frac{1}{2} \boldsymbol{u} \cdot \boldsymbol{u} \; d\Omega = \frac{1}{V_\Omega} \int_\Omega \frac{1}{2} u_i u_i \; d\Omega, \tag{2.11}$$

where $\Omega = [0, L_x) \times [0, L_y) \times [0, L_z)$ and $V_\Omega = L_x L_y L_z$. Starting with a pair of initial conditions that lead to the laminar and turbulent states, and defining suitable upper and lower thresholds on $E(\boldsymbol{u})$ for transition to turbulence (E_T^*) and decay to the laminar state (E_L^*), we can iteratively define new initial conditions that remain near the edge for long times. As the flow is oscillatory in nature, the threshold conditions are met if the average energy of the flow remains above or below these thresholds for a defined time window t_{avg}.

If at time t_0^n we have an initial condition that evolves towards turbulence, $\boldsymbol{u}_T^{n,0}$, and an initial condition that evolves towards the laminar state, $\boldsymbol{u}_L^{n,0}$, then a new initial condition at

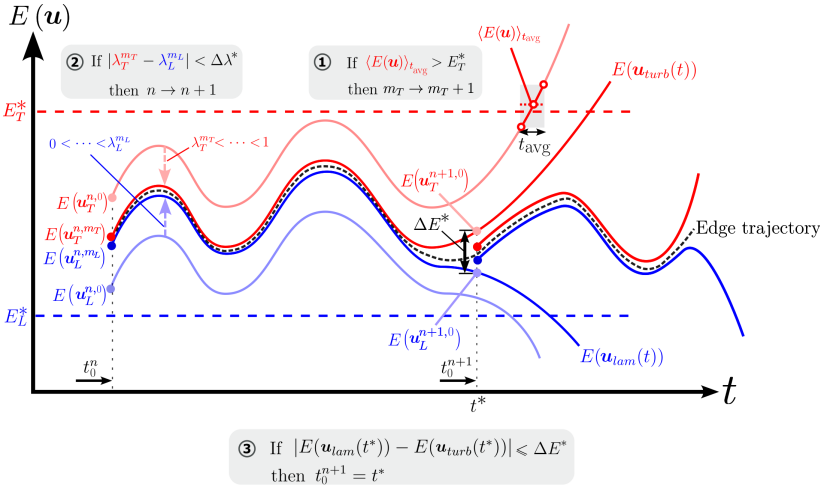

Figure 2: Bisection algorithm scheme. Block 1 indicates that when the energy, averaged over a time window of size t_{avg}, is larger than E_T^* or smaller than E_L^*, then λ is scaled down or up respectively. Block 2 shows that when two consecutive values of λ are closer than $\Delta\lambda^*$, a new starting point is chosen to reinitialise the bisection process. Block 3 shows how the new starting point is chosen. The latest turbulent and laminar trajectories remain nearby for an extended period, until the energy difference between them is larger than ΔE^*. The last time for which the energy difference is below ΔE^* is the new starting point.

this time, $\boldsymbol{u}_\lambda^m$, is defined by linear interpolation:

$$\boldsymbol{u}_\lambda^m = \boldsymbol{u}_L^{n,0} + \lambda_m(\boldsymbol{u}_T^{n,0} - \boldsymbol{u}_L^{n,0}). \tag{2.12}$$

Iterative bisection, enumerated by m, is performed on the parameter λ over the interval [0,1], which generates a set of initial conditions on the laminar and turbulent sides of the edge (λ is increased if the trajectory from $\boldsymbol{u}_\lambda^m$ decays to the laminar state, and decreased if it transitions to turbulence). As the bisection proceeds, the trajectories on either side of the edge spend longer periods of time close to the edge and close to each other. The first pair of initial conditions used to start the bisection process consisted of $\boldsymbol{u}_T^{0,0}$ taken from a minimal seed trajectory (for the definition of a minimal seed, see Kerswell 2018) as it approached the edge state on the turbulent side of the edge manifold (minimal seeds in this problem will be reported at a later date), along with $\boldsymbol{u}_L^{0,0} = \boldsymbol{0}$, the laminar flow state. Results using an alternative initialisation with $\boldsymbol{u}_T^{0,0}$ taken as a random sample of the turbulent flow did not show any qualitative difference; the former option for $\boldsymbol{u}_T^{0,0}$ was chosen when generating a long edge trajectory, owing to efficiencies associated with initialising the algorithm already nearby to the edge.

Once the change in λ between two consecutive iterations is less than a threshold $\Delta\lambda^*$, it is no longer efficient to continue bisecting between the original two initial conditions in (2.12) to track the edge. Instead, a new pair of laminar and turbulent initial conditions for use in (2.12) are generated from the trajectories on either side of the edge. Letting m_L and m_T be the number of initial conditions found on the laminar and turbulent sides of the edge respectively, $\boldsymbol{u}_L^{n,m_L}$ is the most recently found initial condition on the laminar side of the edge, with trajectory $\boldsymbol{u}_{lam}(t)$, and $\boldsymbol{u}_T^{n,m_T}$ is the most recently found initial condition on the turbulent side of the edge, with trajectory $\boldsymbol{u}_{turb}(t)$. We then set a new initial time $t_0^{n+1} = t^*$ and new laminar and turbulent initial conditions for use in (2.12) as $\boldsymbol{u}_L^{n+1,0} = \boldsymbol{u}_{lam}(t^*)$ and

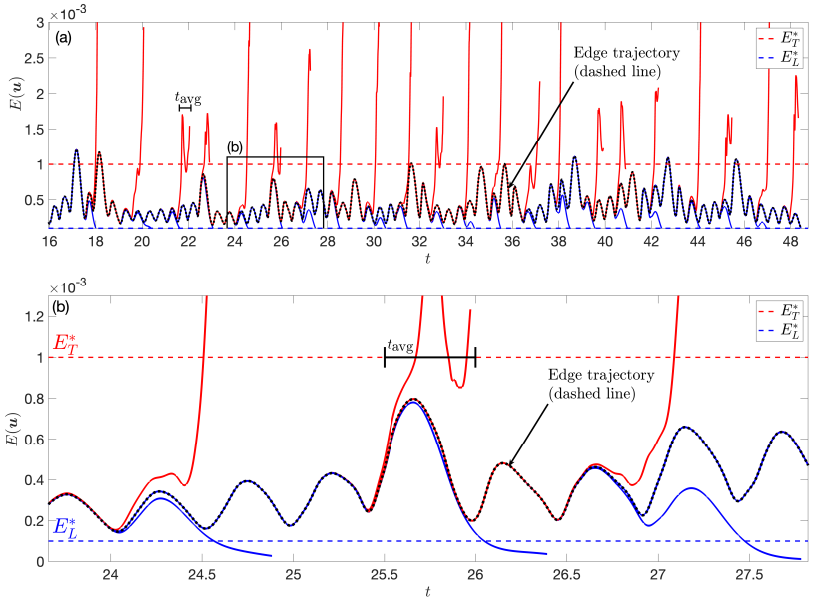

Figure 3: (a) Kinetic energy of the different trajectories bisected to follow the edge. The first (transient) 16 time units of edge tracking are omitted. The red trajectories lead to turbulence and the teal ones relaminarise. The infered edge trajectory shown with a dashed black line. The thresholds for classifying trajectories as laminar (E^*_L) and turbulent (E^*_T) are marked with horizontal dashed lines. The time window over which the energy is averaged is shown near $t = 22$. (b) A detailed version of (a) for $23.5 < t < 28$.

$\boldsymbol{u}_T^{n+1,0} = \boldsymbol{u}_{turb}(t^*)$, where t^* is the last time for which $|E(\boldsymbol{u}_{lam}(t)) - E(\boldsymbol{u}_{turb}(t))| < \Delta E^*$. Different averaging times and threshold values were tested and $t_{avg} = 0.5$, $\Delta\lambda^* = 10^{-4}$, $\Delta E^* = 10^{-6}$, $E^*_L = 10^{-4}$, and $E^*_T = 10^{-3}$ showed to be suitable for achieving an accurate representation of flow dynamics in the vicinity of the edge. These values were determined during the initial stages of investigating the edge trajectory; E^*_T was initially set a little below the turbulent average value (which is readily estimated from a single turbulent simulation), and E^*_L was set very low, at 10^{-8}. These initial values allowed for a short section of edge trajectory to be computed, after which the thresholds were adjusted for efficiency to more closely sandwich the observed edge properties. The values were regularly reviewed to ensure that they were not interfering with the computation of the edge trajectory itself. A schematic representation of the bisection and start time shifting procedure is presented in figure 2.

3. Edge Tracking Results

Following the procedure described in section 2.3, a set of edge trajectories was generated for the baseline simulation, whose energies $E(\boldsymbol{u})$ are shown in figure 3. The results show that, near the edge, the energy is oscillatory with a dominant frequency of $T/2$ caused by the back-and-forth forcing of the wall (see figure 3 (b)). However, the energy on the edge is not periodic (see figure 3 (a)), indicating that the edge state is not a simple periodic orbit, but rather a chaotic saddle, albeit of a strong oscillatory nature. A total simulated time of approximately 50 periods allows for a detailed description of the dynamics on the edge. Here we focus on $t > 16$, after the edge trajectory has settled onto the edge state.

To provide a better understanding of the energy dynamics, an energy evolution equation is derived by projecting (2.2) onto the perturbation velocity field u_i to obtain the local kinetic

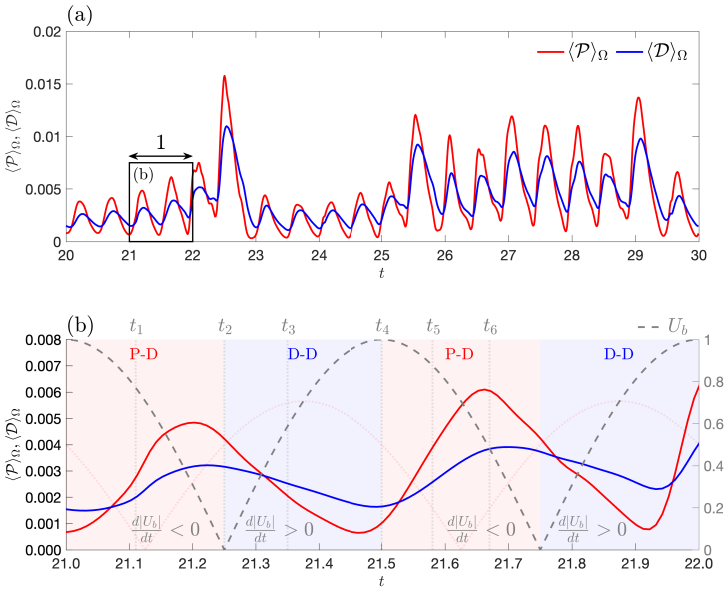

Figure 4: (a) Time-series of production rate (red) and dissipation rate (teal) for $20 < t < 30$. (b) A detailed plot for $21 < t < 22$ showing that within half a period, there is a production-dominated (P-D, red) stage and a dissipation-dominated (D-D, teal) stage. The right-hand axis plots the magnitude of the wall velocity $U_b = U(0,t)$ (grey dashed). The sign of the wall acceleration, $d|U_b(t)|/dt$, is shown to correspond with the P-D and D-D stages. The times of the six snapshots in figure 5 are indicated with dotted lines.

energy density defined as $e = \frac{1}{2}u_i u_i$. The energy transport equation reads

$$\frac{\partial e}{\partial t} = -u_j \frac{\partial p}{\partial x_j} - Re\left[u_i \frac{\partial}{\partial x_j}\left(u_i U_j + u_j U_i + u_j u_i\right)\right] + \frac{\partial^2 e}{\partial x_j \partial x_j} - \frac{\partial u_i}{\partial x_j}\frac{\partial u_i}{\partial x_j}. \tag{3.1}$$

Defining the average operator $\langle\cdot\rangle_{x_i}$ as $\langle a\rangle_{x_i} = \frac{1}{L_{x_i}}\int_0^{L_{x_i}} a\, dx_i$, where $i = 1, 2, 3$ for x, y and z respectively, the total energy E is given by $E = \langle e\rangle_{x,y,z} \equiv \langle e\rangle_\Omega$. Integrating (3.1) over the whole domain, taking into account the boundary conditions and the incompressibility condition (2.1) leads to the global energy balance equation

$$\frac{\mathrm{d}E}{\mathrm{d}t} = \left\langle -Re\, uv \frac{\partial U}{\partial y}\right\rangle_\Omega - \left\langle \frac{\partial u_i}{\partial x_j}\frac{\partial u_i}{\partial x_j}\right\rangle_\Omega \equiv \mathcal{P}(t) - \mathcal{D}(t), \tag{3.2}$$

where $\mathcal{P}(t)$ is the instantaneous production rate, and $\mathcal{D}(t)$ is the instantaneous dissipation rate. The production term has the general form of a stress ($-Re\, uv$) acting on a strain rate ($\partial U/\partial y$), from which the energy transfer process from the laminar velocity gradient (induced by the oscillation) to the perturbation velocity field is clear. Furthermore, the oscillation period of $T/2$ observed in the energy is in agreement with the period T of $\partial U/\partial y$ provided that uv is also periodic with period T (and zero mean).

Figure 4 plots time series of the production and dissipation, and shows that they are in phase, but that there are stages within the $T/2$ cycle when production is dominant and stages when the dissipation is dominant. This observation is in broad agreement with previous work on transitional behaviour in the Stokes layer, which indicates a growth of flow disturbances during the deceleration phase (which is, accordingly, a production-dominated phase) and

their decay during the acceleration phase (Ozdemir *et al.* 2014; Luo & Wu 2010). A closer comparison between these observations and the transitional regime of Ozdemir *et al.* (2014) is made in §4.4. The behaviour of the edge trajectory suggests the presence of an internal self-sustained dynamics that balances the energy transfer among structures in the flow. To further understand the dynamics along the edge, figure 5 plots snapshots of $\langle e \rangle_x$ on the y-z plane at times $t_1 = 21.11$, $t_2 = 21.25$, $t_3 = 21.35$, $t_4 = 21.50$, $t_5 = 21.58$, and $t_6 = 21.67$, which cover a total time just over $T/2$.

Figures 5(a-d) (times t_1 to t_4) show a well-defined region in the y-z plane that concentrates most of the kinetic energy of the flow, which modifies its shape and migrates upwards over time. This region is located around (and just above) the instantaneous location of a local maximum in the absolute value of laminar shear, $|\tau_\ell| = |\partial U/\partial y|$, and rises with it. We label this location $y^{\min}_{\tau_\ell}$ (given that $\partial U/\partial y < 0$). In figure 5(d) the region of concentrated kinetic energy reaches a height $y \approx 2$ and begins to spread out. After $t = t_4$ a new region of concentrated energy is formed near the wall, seen in figures 5(e,f) (times t_5 and t_6), and the process repeats, although this new region aligns with the location of maximal *positive* laminar shear, labelled $y^{\max}_{\tau_\ell}$. Figure 5(g) plots the vertical distribution of the x–z averaged energy $\langle e \rangle_{x,z}$ over an extended period of time, demonstrating that this basic $T/2$ cycle repeats indefinitely, with flow structures periodically forming a little above the plate, rising, and dissipating around $y \lesssim 3$.

The location of the flow structures in the spanwise direction varies sporadically in time, as can be seen in figure 5(h), which shows the spanwise distribution of the x–y averaged energy $\langle e \rangle_{x,y}$. The time window studied in figures 5(a-f) contains flow structures located in a region around the centre of the spanwise domain, while the time window between $t = 23$ and $t = 26$ contains the same structures located around the (periodic) spanwise boundaries. This 'jumping' of the structure by an amount $L_z/2$ is characteristic of a spatially localised structure which nevertheless feels the influence of its periodically located neighbours, owing to the domain size L_z being too small for the structure to evolve entirely freely, but large enough for it to appear essentially isolated for extended periods (Khapko *et al.* 2016). These jumps are associated with elevated energy E during a single half-period $T/2$ in figure 3, as there are essentially two structures side by side, and are distributed randomly in time. If the domain size L_z were large enough, then the jumps would presumably cease since the structure can evolve entirely independently, although this may instead induce a spanwise drift (Khapko *et al.* 2013). Nevertheless, we shall treat the structure as an essentially isolated object in the following analysis, as this is a reasonable approximation for much of the flow evolution between jumps.

To provide a more detailed characterisation of the three-dimensional nature of these structures, figures 6(a-d) plot isosurfaces of high-speed streaks ($u_{Smax} = 0.5\max\{u\}$) and low-speed streaks ($u_{Smin} = 0.5\min\{u\}$) at times t_2 to t_5. The x-averaged energy $\langle e \rangle_x$ is shown on the plane $z = 0$, and the height of maximal energy ($y_{\max\{\langle e \rangle_x\}}$) is plotted on the planes $x = 0$ and $z = L_z$. The instantaneous laminar flow profile is shown on the planes $z = 0$ and $z = L_z$ (shifted to be centred at $x = L_x/2$) for reference. These figures show that the streamwise structures are streak-like, and instantaneously (at least visually) carry the majority of the energy of the perturbed flow, as in the self-sustaining process (Hall & Smith 1991; Waleffe 1997). Indeed, the streamwise velocity is $O(1)$ within these streaks whilst typical cross-stream velocities are $O(10^{-3})$. Within a single half-period $T/2$ (times t_1 to t_3), a single streak with $u < 0$ dominates the perturbation energy. In the following half-period (t_4) the streak is replaced by one of the opposite sign ($u > 0$) and the dynamics of the new streak are essentially the same as the first. This goes some way to explaining the apparent $T/2$ period within the energy budget; the flow itself has a period of T, but the reflection symmetry

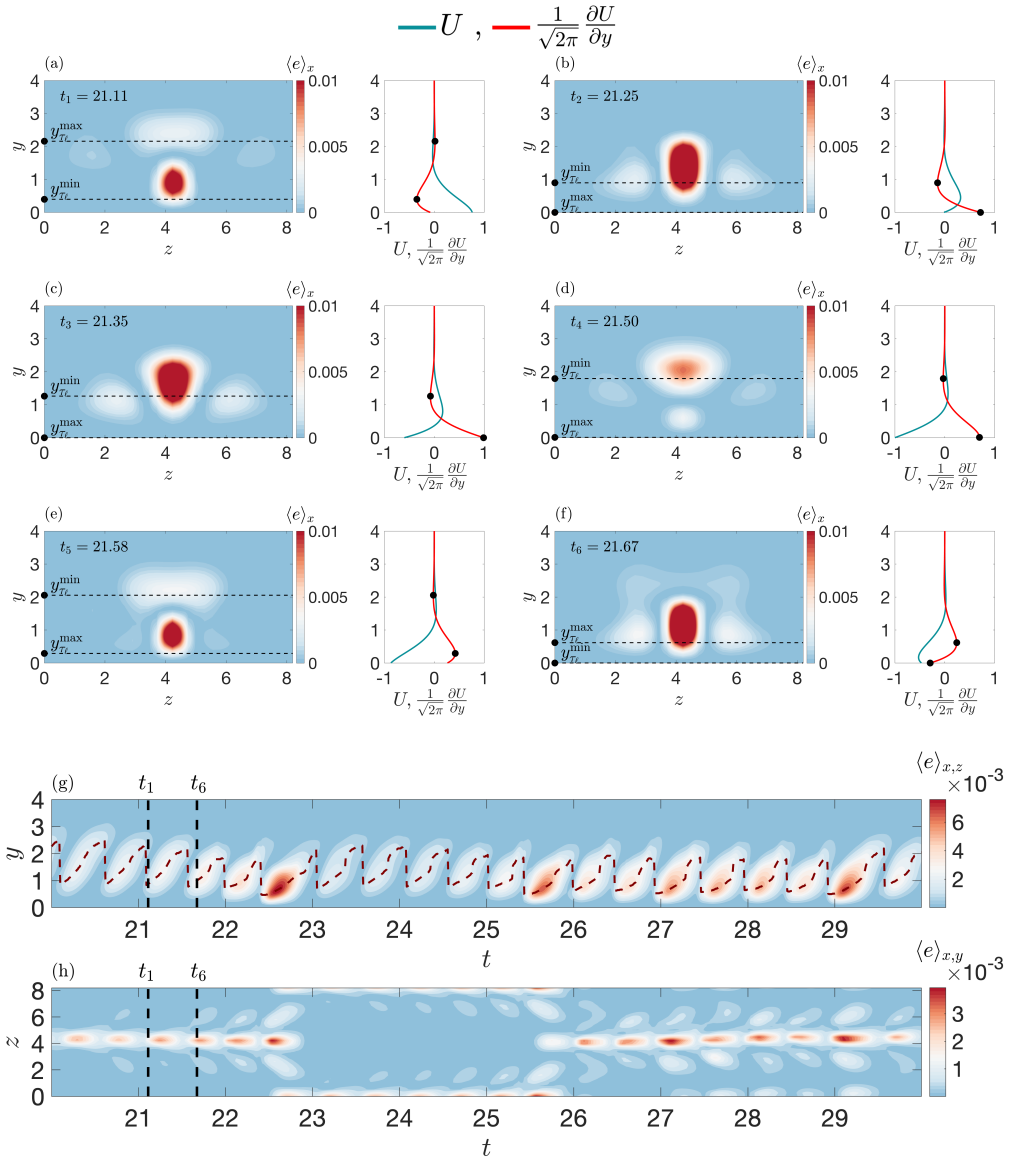

Figure 5: (a-f) Snapshots of $\langle e \rangle_x$ in the y-z plane for six times $t_1 = 21.11$, $t_2 = 21.25$, $t_3 = 21.35$, $t_4 = 21.50$, $t_5 = 21.58$, and $t_6 = 21.67$. The right column of each snapshot shows the corresponding instantaneous laminar velocity U (teal) and normalised shear $(2\pi)^{-1/2}(\partial U/\partial y)$ (red) with black dots at its maximum and minimum. (g) Time-evolution of the average vertical distribution of energy $\langle e \rangle_{x,z}$ and its instantaneous maximum (red dashed). (h) Average spanwise distribution of energy $\langle e \rangle_{x,y}$.

after a time $T/2$ results in pre-periodic motions that are not apparent in positive-definite quantities such as the energy.

Figure 6(e) shows the instantaneous vertical distribution of the x–z-averaged kinetic energy, $\langle e \rangle_{x,z}$, along with the locations of its global maximum and oblique lines of slope

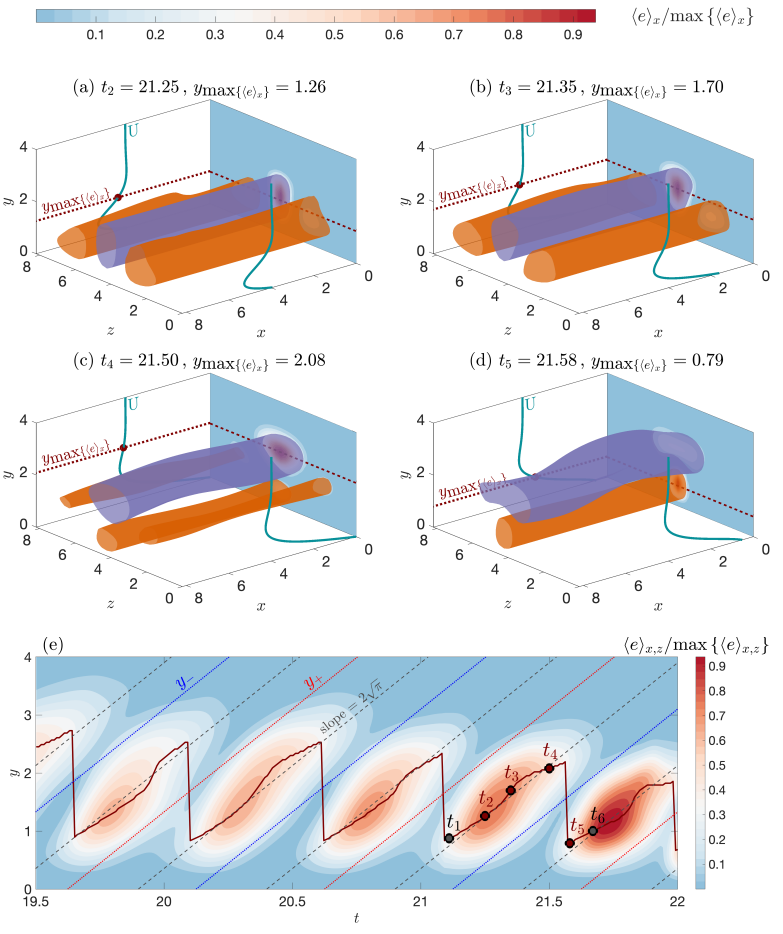

Figure 6: (a-d) Snapshots of high-speed ($u_{Smax} = 0.5\max\{u\}$, purple) and low-speed ($u_{Smin} = 0.5\min\{u\}$, orange) streamwise velocity isosurfaces, at times $t = t_2, t_3, t_4$, and t_5. Streamwise-averaged perturbation energy $\langle e\rangle_x$ is plotted on the plane $z = 0$. The instantaneous height of maximum perturbation energy ($y_{\max\{\langle e\rangle_x\}}$) is plotted on the planes $x = 0$ and $z = L_z$ with a dotted line. The instantaneous laminar flow is plotted on the planes $z = 0$ and $z = L_z$ (centred at $x = L_x/2$). (e) Time evolution of the x, z-averaged perturbation energy $\langle e\rangle_{x,z}$, its instantaneous global maximum (continuous line), and oblique lines (dashed) with slope $2\sqrt{\pi}$. Dotted teal and red lines indicate locations of zero laminar shear, labelled y_+ and y_-, defined in section 4.1.

$2\sqrt{\pi}$, showing that the laminar flow propagation speed controls the spatial location of these nonlinear structures on the edge. The no-slip boundary condition ($\boldsymbol{u} = 0$ at $y = 0$) prevents the streaks from forming at the wall, and instead they begin to form around $y \approx 1/4$ and reach substantial amplitude at $y \approx 1$. As the streaks migrate upwards, they begin to lose a substantial amount of energy around $y \approx 2$ and essentially do not propagate into $y \gtrsim 3$ (this will be demonstrated explicitly in the following section). Although the laminar flow, and hence also the energy production rate $\mathcal{P}$, decays exponentially away from the wall, there is nothing inherently preventing these streaks from continuing to propagate to $y \to \infty$ while viscously decaying through $\mathcal{D}$; therefore, there must be some further dynamics contained within the other flow components that essentially cut-off the streaks beyond a maximum height. The exact physical mechanisms driving these observations will be explained in the

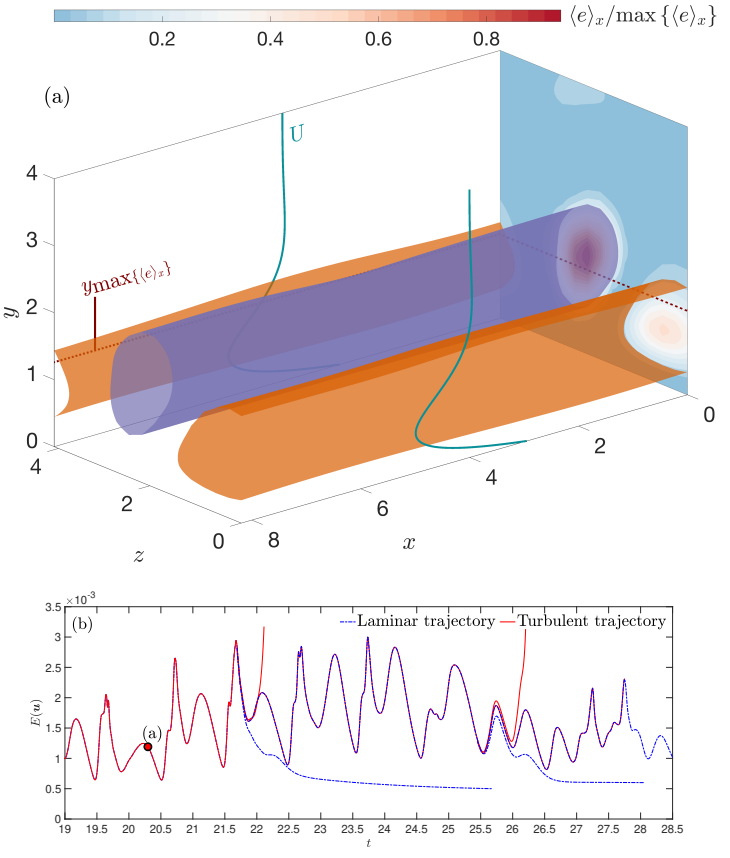

Figure 7: (a) Snapshot at $t = 20.35$ of high and low speed streaks, as in figure 6 for the narrower domain. (b) The corresponding perturbation energy from edge tracking.

following section. A supplementary movie accompanying figure 6 is available, which shows the streak dynamics and includes a jump of the streaks from the centre of the domain to the spanwise boundaries.

Edge tracking was also performed at a higher Reynolds number of $Re = 1200$ using the same computational setup, and the dynamics were quantitatively similar to those at $Re = 1000$. Due to the moderate Reynolds numbers used and the small gap between them, no clear scaling of flow structures with Re was observed. Another set of edge tracking results were computed in a narrower domain with half the spanwise extent ($L_z = 4.1$, using the same spatial and temporal resolution) for $Re = 1000$, to see whether or not a truly periodic edge state could be identified. However, the edge trajectory in this case is significantly more chaotic than in the wider domain, and no period of nearly periodic motion can be identified for further analysis of the flow structures. Figure 7 shows a snapshot of the flow in the narrow domain, from which it is seen that the structures are similar to those of the wider domain discussed above. However, the flow is too confined, and alternating signed streaks 'compete' for space as they form and migrate upwards, and a consistent pattern of dynamics does not clearly emerge. The next section will focus entirely on the wide domain with $Re = 1000$ and demonstrate that rolls in the y–z plane, which sustain the streamwise streaks during their migration, span the entire domain, and it is likely that these rolls do not have enough room in the narrow domain to establish a sustained periodic flow.

4. The Periodic Self Sustained Process (PSSP)

To fully understand the streak dynamics, including their creation, migration, growth, and sudden decay, we analyse the effect of wall-oscillation on the self sustaining process, by decomposing the full perturbation velocity into its streak, roll and wave (SRW) components. The average of the velocity field over the x-direction, $\boldsymbol{\mathcal{U}} = \langle \boldsymbol{u} \rangle_x$, can be decomposed into streak and roll components as $\boldsymbol{\mathcal{U}} = \boldsymbol{\mathcal{U}}_s + \boldsymbol{\mathcal{U}}_r \equiv (\mathcal{U}, 0, 0)_s + (0, \mathcal{V}, \mathcal{W})_r$. The full perturbation velocity field can be expressed as

$$\boldsymbol{u} = \boldsymbol{\mathcal{U}}_s + \boldsymbol{\mathcal{U}}_r + \hat{\boldsymbol{u}} = (\mathcal{U}, 0, 0)_s + (0, \mathcal{V}, \mathcal{W})_r + (\hat{u}, \hat{v}, \hat{w})_w \tag{4.1}$$

where the subscript s denotes the streak velocity, the r subscript denotes the roll velocity, and the w subscript and hat decoration denotes the remaining part of the fully three-dimensional velocity field. Introducing this decomposition into (2.2), we obtain momentum equations for $\mathcal{U}$, $\mathcal{V}$, and $\mathcal{W}$:

$$\frac{\partial \mathcal{U}}{\partial t} + Re\ \mathcal{U}_j \frac{\partial \mathcal{U}}{\partial x_j} = -Re \left\{ \mathcal{V} \frac{\partial U}{\partial y} + \frac{\partial \left\langle \hat{u}\hat{u}_j \right\rangle_x}{\partial x_j} \right\} + \frac{\partial^2 \mathcal{U}}{\partial x_j \partial x_j}, \tag{4.2}$$

$$\frac{\partial \mathcal{V}}{\partial t} + Re\ \mathcal{U}_j \frac{\partial \mathcal{V}}{\partial x_j} = -\frac{\partial \mathscr{P}}{\partial y} - Re \frac{\partial \left\langle \hat{v}\hat{u}_j \right\rangle_x}{\partial x_j} + \frac{\partial^2 \mathcal{V}}{\partial x_j \partial x_j}, \tag{4.3}$$

$$\frac{\partial \mathcal{W}}{\partial t} + Re\ \mathcal{U}_j \frac{\partial \mathcal{W}}{\partial x_j} = -\frac{\partial \mathscr{P}}{\partial z} - Re \frac{\partial \left\langle \hat{w}\hat{u}_j \right\rangle_x}{\partial x_j} + \frac{\partial^2 \mathcal{W}}{\partial x_j \partial x_j}, \tag{4.4}$$

where $\mathscr{P} \equiv \langle p \rangle_x$ is the the x-averaged pressure. Mass conservation within the SRW decomposition reads

$$\frac{\partial \mathcal{V}}{\partial y} + \frac{\partial \mathcal{W}}{\partial z} = 0 \quad \text{and} \quad \frac{\partial \hat{u}_i}{\partial x_i} = 0, \tag{4.5}$$

and momentum equations for the wave components $\hat{\boldsymbol{u}}$ can be obtained by subtracting (4.2–4.4) from (2.2), though the resulting equations are not needed here.

4.1. *Cycle description and energy transport dynamics*

To unveil the dynamics among streaks, rolls and waves, we analyse the evolution of the energy within the SRW-decomposition. Defining the streak energy density as $\mathcal{E}_s \equiv \frac{1}{2}\mathcal{U}^2$, the roll energy density as $\mathcal{E}_r \equiv \frac{1}{2}(\mathcal{V}^2 + \mathcal{W}^2)$, and the x-averaged wave energy density as $\hat{\mathcal{E}} \equiv \langle \frac{1}{2}|\hat{\boldsymbol{u}}|^2 \rangle_x$, we have by construction that the x-averaged total perturbation energy density $\mathcal{E} \equiv \langle e \rangle_x$ is given by $\mathcal{E} = \mathcal{E}_s + \mathcal{E}_r + \hat{\mathcal{E}}$, given that the cross-terms vanish. The SRW equations (4.2–4.4) may be converted into evolution equations for the streak energy density and roll energy density, and an equation for the x-averaged wave energy density can be constructed by observing that $\frac{\partial \hat{\mathcal{E}}}{\partial t} = \frac{\partial \mathcal{E}}{\partial t} - \frac{\partial \mathcal{E}_s}{\partial t} - \frac{\partial \mathcal{E}_r}{\partial t}$. These equations are presented in appendix A.

The energy density evolution equations contain flux terms which move energy within the domain, in addition to production from the laminar flow, transfer between rolls, streaks and waves, and dissipation terms. To better elucidate the key mechanisms sustaining the motion, we integrate the equations over the whole domain to give evolution equations for the total

streak $E_s = \langle \mathcal{E}_s \rangle_\Omega$, roll $E_r = \langle \mathcal{E}_r \rangle_\Omega$, and wave $\hat{E} = \langle \hat{\mathcal{E}} \rangle_\Omega$ energies:

$$\frac{\mathrm{d}E_s}{\mathrm{d}t} = \langle \mathcal{P}_{\ell \to s} \rangle_\Omega - \langle \mathcal{T}_{s \to w} \rangle_\Omega - \langle \mathcal{D}_s \rangle_\Omega, \tag{4.6}$$

$$\frac{\mathrm{d}E_r}{\mathrm{d}t} = \langle \mathcal{T}_{w \to r} \rangle_\Omega - \langle \mathcal{D}_r \rangle_\Omega, \tag{4.7}$$

$$\frac{\mathrm{d}\hat{E}}{\mathrm{d}t} = \langle \mathcal{P}_{\ell \to w} \rangle_\Omega + \langle \mathcal{T}_{s \to w} \rangle_\Omega - \langle \mathcal{T}_{w \to r} \rangle_\Omega - \langle \mathcal{D}_w \rangle_\Omega. \tag{4.8}$$

The production ($\mathcal{P}$), transfer ($\mathcal{T}$), and dissipation ($\mathcal{D}$) terms are also given in appendix A. Their indices indicate the source and the destination of the transferred energy (in the case of $\mathcal{P}$ and $\mathcal{T}$) or the component which is dissipating energy (in the case of $\mathcal{D}$), where the laminar flow is denoted by ℓ. For example, the term

$$\mathcal{P}_{\ell \to s} \equiv -Re\mathcal{U}\mathcal{V}\frac{\partial U}{\partial y} \tag{4.9}$$

corresponds to the production of perturbation energy by the laminar flow, creating streaks $\mathcal{U}$ (and mediated by the vertical roll component $\mathcal{V}$). This is the process that creates streaks via the so-called *lift-up mechanism*, which forms part of the Self-Sustaining Process (SSP) (Waleffe 1997). The volume-average of each energy component in equations (4.6–4.8) are plotted in figure 8 along with the total energy E whose evolution in terms of these components is

$$\frac{\mathrm{d}E}{\mathrm{d}t} = \mathcal{P}(t) - \mathcal{D}(t) \equiv (\langle \mathcal{P}_{\ell \to s} \rangle_\Omega + \langle \mathcal{P}_{\ell \to w} \rangle_\Omega) - (\langle \mathcal{D}_\ell \rangle_\Omega + \langle \mathcal{D}_r \rangle_\Omega + \langle \mathcal{D}_w \rangle_\Omega). \tag{4.10}$$

Figure 8 clearly shows a scale difference in energy and energy transfer rate terms between rolls, streaks and waves. Figure 8(a) shows that the most energetic component is the streaks, with energy that is almost indistinguishable from the total energy. The second most energetic structures are the waves, which have an average energy around one and a half orders of magnitude smaller than the streaks, and the rolls are the least energetic structures with average energy around two orders of magnitude smaller than the streaks. This hierarchy is as expected from vortex-wave interaction theory (Hall & Smith 1991), albeit with relative sizes that don't match the high Reynolds number asymptotic theory, owing to the relatively modest Reynolds number used here (see Hall & Sherwin 2010).

Figure 8(b) shows that the scale differences persist among the energy transfer terms. The largest two terms in the energy budget are the production term transferring energy from the laminar flow to the streaks through the lift-up mechanism, $\langle \mathcal{P}_{\ell \to s} \rangle_\Omega$, and the streak dissipation, $\langle \mathcal{D}_s \rangle$, which dissipates most of this energy, and is almost exactly in phase with and of the same magnitude as $\langle \mathcal{P}_{\ell \to s} \rangle_\Omega$. The small amount of streak energy gained from production which is not dissipated is transferred to the waves via $\langle \mathcal{T}_{s \to w} \rangle_\Omega$. This transfer rate is around an order of magnitude smaller than the streak production and dissipation, and is responsible for powering the smaller amplitude waves. In turn, this energy transfer to the waves is balanced almost entirely by the wave dissipation $\langle \mathcal{D}_w \rangle_\Omega$, which is of a similar magnitude as $\langle \mathcal{T}_{s \to w} \rangle_\Omega$ and in phase with it. The waves receive little energy via production from the laminar flow, $\langle \mathcal{P}_{\ell \to w} \rangle_\Omega$. This production term oscillates somewhat randomly between positive and negative values (backscatter onto the laminar flow) and essentially averages to zero over long periods of time; the laminar flow is stable to linear waves at this Reynolds number (and in this geometry). This production term essentially plays no meaningful role in the wave dynamics as its average magnitude is around an order of magnitude smaller than either the transfer to the waves from the streaks, $\langle \mathcal{T}_{s \to w} \rangle_\Omega$, or the wave dissipation, $\langle \mathcal{D}_w \rangle_\Omega$. The waves lose a small amount of energy to the rolls, via the

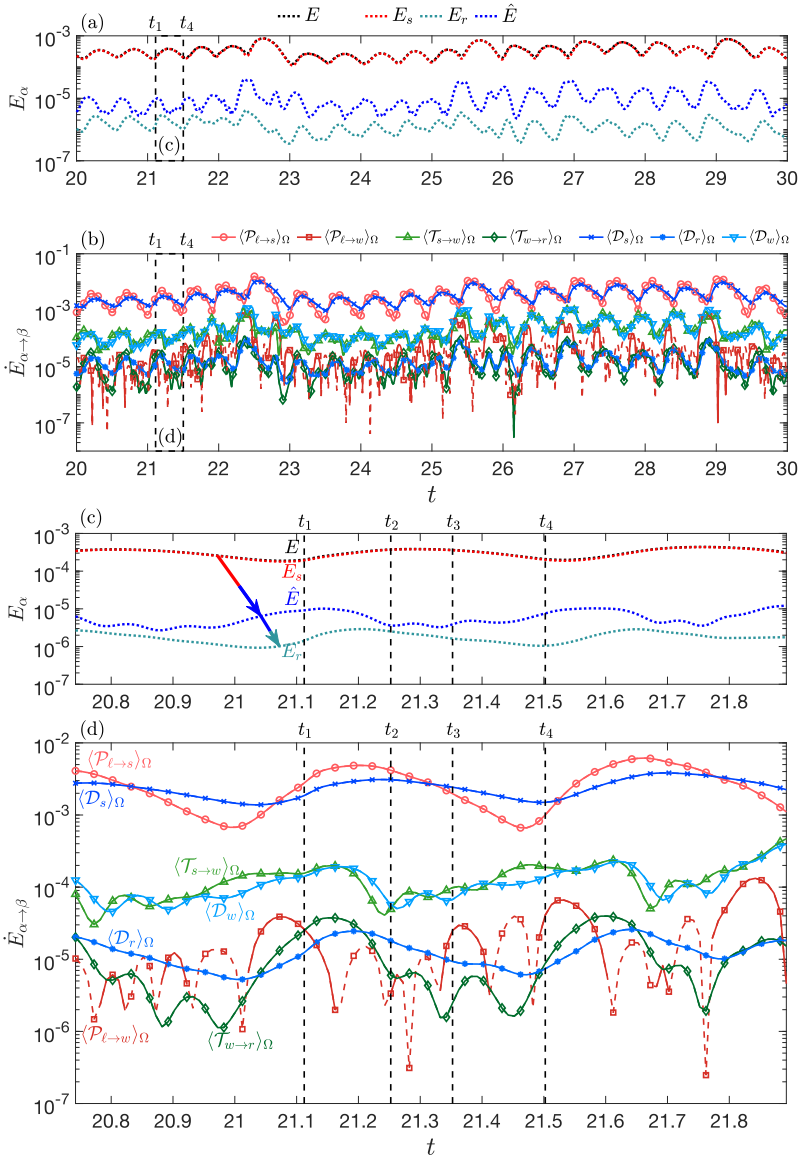

Figure 8: (a) Time series of energy components E_α: E (black), E_s (red), E_r (green), and $\hat{E}$ (teal) . (b) Time series of individual production, transfer, and dissipation terms (labelled $\dot{E}_{\alpha\to\beta}$): $\langle\mathcal{P}_{\ell\to s}\rangle_\Omega$ (light red circles), $\langle\mathcal{P}_{\ell\to w}\rangle_\Omega$ (dark red squares), $\langle\mathcal{T}_{s\to w}\rangle_\Omega$ (light green upwards triangles), $\langle\mathcal{T}_{w\to r}\rangle_\Omega$ (dark green diamonds), $\langle\mathcal{D}_s\rangle_\Omega$ (dark teal crosses), $\langle\mathcal{D}_r\rangle_\Omega$ (mid teal filled circles), and $\langle\mathcal{D}_w\rangle_\Omega$ (light teal downwards triangles). (c-d) The same as (a-b) for $20.75 \leqslant t \leqslant 21.9$. Dashed sections of $\langle\mathcal{P}_{\ell\to w}\rangle_\Omega$ are negative values.

transfer term $\langle\mathcal{T}_{w\to r}\rangle_\Omega$, which is also an order of magnitude smaller than either $\langle\mathcal{T}_{s\to w}\rangle_\Omega$ or $\langle\mathcal{D}_w\rangle_\Omega$. The transfer from the waves to the rolls, $\langle\mathcal{T}_{w\to r}\rangle_\Omega$, is of the same magnitude and nearly in phase with the roll dissipation, $\langle\mathcal{D}_r\rangle_\Omega$.

A closer visualisation of the time series is plotted in figures 8(c,d) for $20.8 \leqslant t \leqslant 22$. In 8(c), it can be seen that the reduction in total streak energy leads to an increment in the total wave energy, which in turn leads to an increment in the total roll energy. The 'cascade'

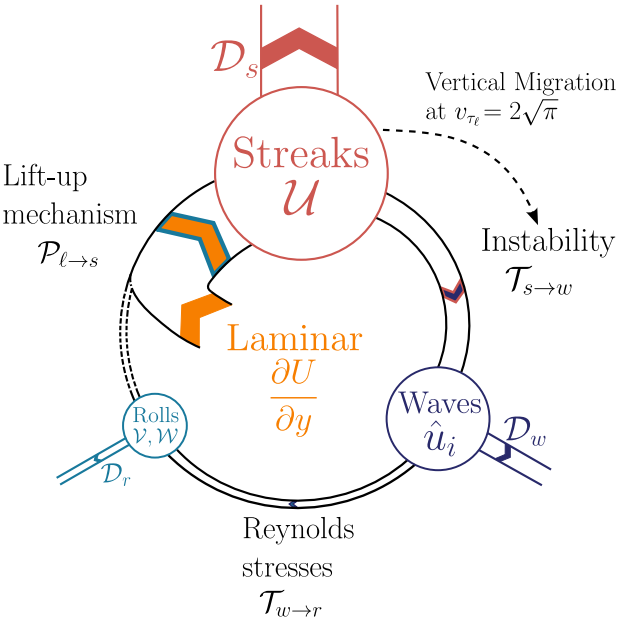

Figure 9: Schematic representation of the energy transfer cycle for the Periodic Self-Sustaining Process (PSSP). The input of energy comes from the laminar flow formed from the plate oscillation. This is transferred to the streaks via the lift-up mechanism due to the action of the rolls (the role of the roles is purely advective; no energy is transferred). Streaks dissipate most of the energy and what remains is is transferred to the waves through linear instability. Waves dissipate most of this energy and transfer what remains to the rolls through Reynolds stresses and the cycle repeats.

process is indicated with a tri-coloured arrow in the plot, and indicates that the energy transfers first between the streaks and the waves, and second between the waves and the rolls. Furthermore, as the rolls begin to gain energy, there is a subsequent increase in the streak energy, as expected from the lift-up mechanism, and the cycle repeats. In summary, each flow component receives and loses the majority of its energy from a single source, as in the SSP of Waleffe (1997), but the periodic nature of the structures presented here more readily reveals the flow of energy through the system than in other, steady, realisations of the SSP. Additionally, it is often not made explicit that most of the energy at every step of the SSP is dissipated, with only a little being transferred to the next part of the cycle; the largest sink of energy is the streaks and the smallest is the rolls. This cycle is presented schematically in figure 9, which echoes the well-known figure of (Waleffe 1997), but includes energy sinks (dissipation) and indicates the main flow of energy using different pathway thicknesses and circle sizes for each component of the flow.

This view of the global energies and energy transfer rates does not provide any information on the mechanistic flow processes and flow structures involved in this cycle. It also does not explain exactly how the flow manages to organise itself periodically, for example why the nonlinear streaks move upward at a speed dictated by the linear laminar flow, why they stop after a finite distance, and how the waves and rolls manage to create further streaks close to the wall. An explanation based upon the spatial evolution of the various flow components and spatial distribution of the energy transfer rates during the cycle is needed.

4.2. *Streak and roll dynamics*

Figure 10 shows the distribution in the y–z plane of the energy transfer components $\mathcal{P}_{\ell\to s}$, $\mathcal{D}_s$, $\mathcal{T}_{w\to r}$, and $\mathcal{D}_r$, which are responsible for supplying and dissipating energy within the streaks and rolls, at the times t_1, t_2, t_3, and t_4 indicated in figure 8(c,d). Overlain on each panel are instantaneous roll streamlines and contours of high streak energy ($\mathcal{E}_s \geqslant 0.25 \max_\Omega \{\mathcal{E}_s\}$). The laminar velocity and (scaled) shear profiles are displayed in the right column of the plot to relate the stage of the Periodic Self-Sustaining Process (PSSP) with the stage of the wall oscillation. These profiles are plotted alongside the normalised strain-rate magnitude of the rolls, whose magnitude is defined as

$$|\mathcal{S}| = Re\sqrt{2\left[\left(\frac{\partial \mathcal{V}}{\partial y}\right)^2 + \frac{1}{2}\left(\frac{\partial \mathcal{V}}{\partial z} + \frac{\partial \mathcal{W}}{\partial y}\right)^2 + \left(\frac{\partial \mathcal{W}}{\partial z}\right)^2\right]}, \tag{4.11}$$

which is normalised via $|\mathcal{S}^*| = |\mathcal{S}|/\max_\Omega\{\mathcal{S}\}$.

The roll streamlines in figure 10 show that the overall shape of the rolls is persistent throughout the time interval $t_1 \leqslant t \leqslant t_4$, forming recirculation cells of $O(1)$ size. These cells only slightly modify their shape over time, remaining located in the same areas throughout the cycle; their magnitude alone oscillates in time. They form a narrow channel around $z \approx L_z/2$ of upward roll velocity, and the streaks form, grow, and migrate upward in this channel. The channel ends at a stagnation point (in the y–z plane) around $y = y_{SP} \lesssim 3$ which appears to present a barrier for the upward migrating streak. The roll velocity is horizontal away from the stagnation point at $(y, z) \approx (y_{SP}, L_z/2)$ and gradually turns upward, or downward back towards the wall, at the spanwise extremities of the domain.

It is apparent from the roll structure that the streaks reside largely in a region for which $\mathcal{V} > 0$ around $z = L_z/2$ below the stagnation point at $y = y_{SP}$. In order for the streak production rate $\mathcal{P}_{\ell\to s} = -Re\mathcal{U}\mathcal{V}\partial U/\partial y$ to be positive in this region, we therefore require that the combination $\mathcal{U}\partial U/\partial y < 0$ since the sign of $\mathcal{V}$ is fixed. As such, a positive streak ($\mathcal{U} > 0$) can only grow when the laminar shear is negative ($\partial U/\partial y < 0$) and *vice versa*. This observation, along with the fact that the laminar flow $U(y, t)$ is periodic, and that its features propagate upward at a speed $2\sqrt{\pi}$, goes some way to explaining the streak migration.

To make this notion precise, we detail key features of the laminar profile. Heights with zero laminar shear are denoted $y_\pm$ such that the laminar shear transitions from negative to positive through y_+ (i.e. $\partial^2 U/\partial y^2|_{y=y_+} > 0$) and *vice versa*. Locations of maximum and minimum laminar shear are denoted $y^*_\pm$. This notation is illustrated in figure 11. We introduce the cycle time $0 \leqslant \xi < 1$, where the total time is $t = kT + \xi$ with $T = 1$ and k an integer, and consider the evolution of $y_\pm(\xi)$ and $y^*_\pm(\xi)$. A laminar shear minima appears at the wall when $\xi = 0$ and for $0 \leqslant \xi < 1$ is located at $y^*_-(\xi) = 2\sqrt{\pi}\xi$. After half a cycle, at $\xi = T/2 = 1/2$, a laminar shear maxima appears at the wall and for $1/2 \leqslant \xi < 1$ is located at $y^*_+(\xi) = \sqrt{\pi}(2\xi - 1)$. Above the wall at the beginning of the cycle, the laminar shear changes sign at $y_+ = 3\sqrt{\pi}/4$. As time advances, this location of zero shear is given by $y_+(\xi) = \sqrt{\pi}(2\xi + 3/4)$. When $\xi = 1/8$, another location where the laminar shear changes sign appears at the wall, and for $1/8 \leqslant \xi < 1$ is located at $y_-(\xi) = \sqrt{\pi}(2\xi - 1/4)$. When $\xi = 5/8$, a final zero shear location appears at the wall and its location is given by $y_+(\xi) = \sqrt{\pi}(2\xi - 5/4)$.

These locations are illustrated at four times within the cycle in figure 11. They divide the region around $z \approx L_z/2$ below the stagnation point into locations where the production term $\mathcal{P}_{\ell\to s}$ can create positive streaks ($\partial U/\partial y < 0$, coloured pink) and locations where it can create negative streaks ($\partial U/\partial y > 0$, coloured teal). These regions are also overlain on the energy transfer term distributions and laminar flow profiles in figure 10. The schematics in figure 11 make a further distinction within each region; for a substantial production term we

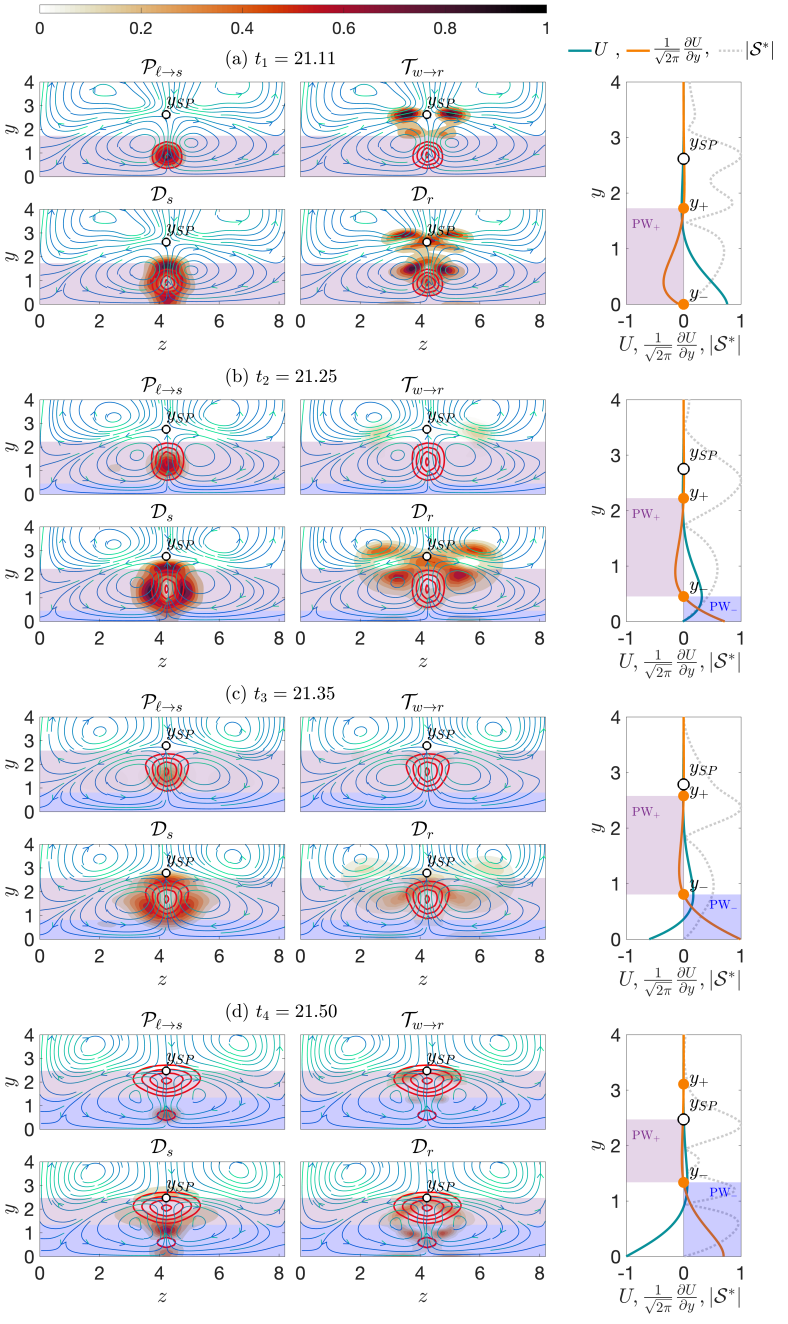

Figure 10: Distribution in the y–z plane of the energy transfer components $\mathcal{P}_{\ell\to s}$, $\mathcal{T}_{w\to r}$, $\mathcal{D}_s$, and $\mathcal{D}_r$ at times t_1 to t_4, normalised by each of their maximum values across the time window $t_1 \leqslant t \leqslant t_4$. Roll streamlines are coloured by the local roll energy. Red contour lines show high streak energy ($\mathcal{E}_s \geqslant 0.25 \max_\Omega \{\mathcal{E}_s\}$). Shaded Production Windows are shown for negative and positive streaks (PW$_-$, teal, and PW$_+$, pink). The right-hand column shows the laminar velocity (green) and normalised shear (orange) along with the normalised roll strain rate $\mathcal{S}^*$ (grey dashed) defined in (4.11).

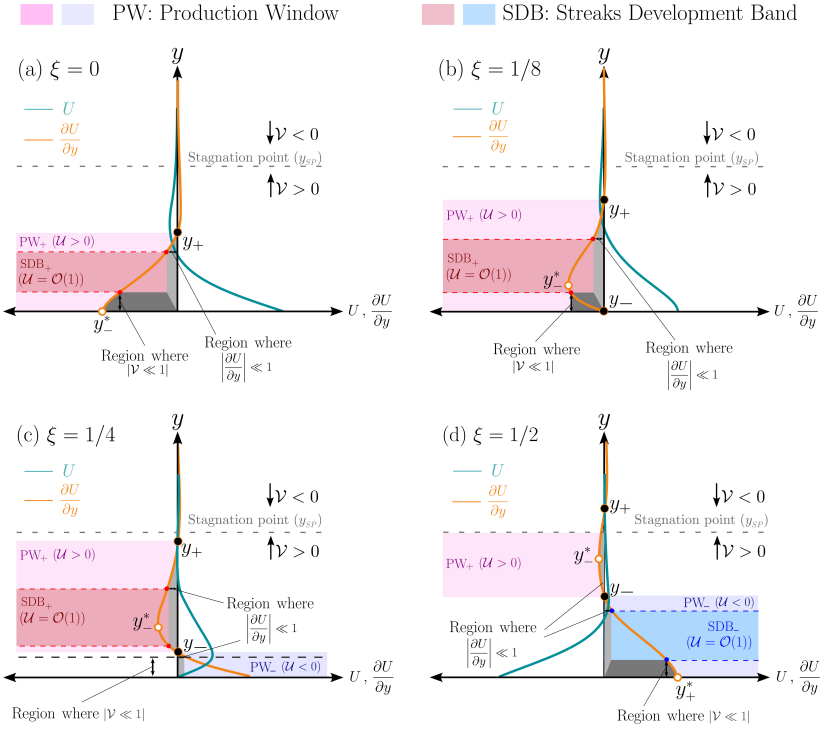

Figure 11: Schematics of four different stages of the streak development and upward migration at the centreline between the roll recirculation cells. Light red and teal represent Production Windows (PWs), regions of the flow where the production term $\mathcal{P}_{\ell\to s}$ is positive. In darker red and teal, Streaks Development Bands (SDBs) are presented. These are subregions of the PWs where $\mathcal{P}_{\ell\to s}$ is of substantial size, and therefore regions where streaks develop. The PWs and SDBs migrate upwards at a speed of $2\sqrt{\pi}$ according to the locations of $y_\pm(\xi)$ defined in the text and can sustain positive (PW$_+$, SDB$_+$, $\mathcal{U} > 0$) and negative (PW$_-$, SDB$_-$, $\mathcal{U} < 0$) streaks. In (a), there is a PW$_-$ between y_+ and y_{SP} which is intentionally omitted for clarity of the discussion.

require that both $\partial U/\partial y$ and $\mathcal{V}$ are large enough to provide a meaningful energy input to the streaks. We therefore expect to have reduced streak growth around $y = y_\pm$ (where $\partial U/\partial y$ is small) and around $y = 0$ (where $\mathcal{V}$ is small). This defines 'Streak Development Bands' (SDBs) which are indicated with a darker shade in figure 11.

To relate this scheme to the dynamics observed in figure 10, at the beginning of the cycle ($\xi = 0$) the region $0 < y < y_+(0) = 3\sqrt{\pi}/4$ has negative laminar shear $\partial U/\partial y < 0$ and positive vertical roll velocity $\mathcal{V} > 0$ around $z \approx L_z/2$, meaning that a positively-signed streak ($\mathcal{U} > 0$) grows in this region. However, due to the no-slip condition at $y = 0$ (the boundary conditions ensure that $\mathcal{V} \propto y^2$ near the wall), $\mathcal{V}$ is too weak near the wall to produce large values of $\mathcal{P}_{\ell\to s}$. The streak therefore grows to a spatial extent of $\mathcal{O}(1)$ within a Streak Development Band (SDB), with its lower edge a little separated from the wall.

A little after the beginning of the cycle, at $\xi_1 = 0.11$, the laminar shear maxima $y^*_-(\xi)$ has moved upwards to the lower edge of the streak, as shown in figure 10(a). At this time, the streak has essentially not moved from its initial position at $\xi = 0$, but has become stronger and larger (*c.f.* figures 8(c) and 6(e) respectively) and the production $\mathcal{P}_{\ell\to s}$ is centred in the middle of the streak. There is substantial dissipation $\mathcal{D}_s$ in a ring around the streak, owing to increased streak velocity gradients.

The total streak dissipation is lower than the total production ($\langle\mathcal{D}_s\rangle_\Omega < \langle\mathcal{P}_{\ell\to s}\rangle_\Omega$) for

$\xi_1 \leqslant \xi \leqslant \xi_2 = 0.25$ and so the streak continues to grow in magnitude during this period. However, it starts to migrate upwards, as do the concentrations of $\mathcal{D}_s$ and $\mathcal{P}_{\ell\to s}$, as can be seen in figure 10(b). After $\xi = 1/8$, the region $0 \leqslant y < y_-(\xi)$ has *positive* laminar shear $\partial U/\partial y > 0$ and positive vertical roll velocity $\mathcal{V} > 0$, so that any positively-signed streak velocity $\mathcal{U} > 0$ in this region experiences *negative* production $\mathcal{P}_{\ell\to s}$, i.e. the lift-up mechanism acts to destroy the streak in $0 \leqslant y < y_-(\xi)$. This ultimately means that the streak cannot exist (with a significant amplitude for any significant period of time) outside of $y_-(\xi) < y < y_+(\xi)$. This region with positive production migrates upward at speed $\mathrm{d}y_-/\mathrm{d}\xi = \mathrm{d}y_+/\mathrm{d}\xi = 2\sqrt{\pi}$, and hence so does the streak. Interestingly, the streak advection term $Re\mathcal{V}\partial\mathcal{U}/\partial y$ in (4.2) has an advection velocity $Re\mathcal{V}$ around 2 to 3 times larger than $2\sqrt{\pi}$ within and around the streak (depending on the time during the cycle), so that the streak is effectively hindered from migrating upward with the roll advection since any part of the streak crossing the upper edge of the SDB at y_+ is subject to destruction from $\mathcal{P}_{\ell\to s} < 0$.

As this upward migration proceeds, the magnitude of the laminar shear decreases exponentially in time; within $y_-(\xi) < y < y_+(\xi)$, we have $|\partial U/\partial y| \leqslant \sqrt{\pi}e^{-2\xi}$. The streak energy saturates at a time $\xi_2 < \xi < \xi_3 = 0.35$ (see figure 8(c)) and at ξ_3 the total streak dissipation is larger than the production ($\langle\mathcal{D}_s\rangle_\Omega > \langle\mathcal{P}_{\ell\to s}\rangle_\Omega$). Throughout the period of growth and uplift, $\xi_1 < \xi < \xi_3$, the centre of the streak and its production remain above the location of the minimum laminar shear, $y^*_-(\xi)$. Instead, the streak centres itself in the middle of the production region $y_-(\xi) < y < y_+(\xi)$. This can be seen in figures 10(b,c) in which $y^*_-(\xi)$ is located around a quarter of the way up the streak (it is straightforward to show that $y_+ - y_- = 4(y^* - y_-)$).

However, the ultimate fate of the streak is not to be gradually lost to dissipation while continuing to move upwards as the production rate continues to decrease exponentially. Instead, the upward migration of the production window $y_-(\xi) < y < y_+(\xi)$ eventually moves the centre of the streak on top of the roll velocity stagnation point, see figure 10(d) at $\xi_4 = 0.5$. The streak is essentially ripped apart in the stagnation point due to the high strain rate in this region (a peak of global strain-rate magnitude is observed around the stagnation point in figure 10 (a-d) and its magnitude is around 15 when the streak crosses it), substantial wave activity is created (see figure 8(c,d)), and the local streak dissipation rapidly destroys what remains. Meanwhile, a new streak is formed close to the wall, below $y_-(\xi_4) = 3\sqrt{\pi}/4$, in which the laminar shear is *positive* ($\partial U/\partial y > 0$) and the vertical roll velocity is (still) positive ($\mathcal{V} > 0$), and so the production term $\mathcal{P}_{\ell\to s}$ produces a *negatively*-signed streak in this region ($\mathcal{U} < 0$). The cycle then repeats itself during $0.5 \leqslant \xi < 1$, with the sign of the streak reversed from the description above.

This description of the streak cycle predicates that the roll velocity magnitude is sufficient for the lift-up mechanism to act against the laminar shear in the correct way. The rolls are sustained by energy transfer from the waves ($\mathcal{T}_{w\to r}$), and dissipate energy in regions where vertical and spanwise velocity gradients are concentrated ($\mathcal{D}_r$). Figures 10(a-c) show that the roll dissipation is concentrated around the stagnation point in a 'figure eight' pattern throughout most of the cycle. This is the location where the streamlines change direction from vertical to horizontal most rapidly, and therefore where the largest gradients are expected to be located. The magnitude of the dissipation decreases from ξ_1 to ξ_4. At the end of the (single) streak cycle, $\xi = \xi_4 = 0.5$, there is also dissipation in the area between the old streak and the new streak, within which $\mathcal{W}$ changes sign. This dissipation region is also present at time ξ_1, between the previous streak and the new streak that has just developed.

Just after the beginning of the cycle, at ξ_1, there is a peak in the transfer from the waves to the rolls, $\mathcal{T}_{w\to r}$ (figure 10(a)). This is from wave activity associated with the final destruction of the previous streak at the stagnation point. As such, the energy transfer from waves to rolls is concentrated around the stagnation point, and acts primarily to accelerate the rolls

horizontally ($\mathcal{W}$) away from the stagnation point. This energy transfer takes the form of a wave Reynolds stress (see appendix A), and a detailed description of which terms contribute to this Reynolds stress is given in the next section. Mass conservation ensures that this local forcing enhances the rotation of the entirety of the cells, and concentrates the streamlines within the stagnation point. At the intermediate times ξ_2 and ξ_3, the energy transfer from the waves decays (figure 10(b,c) which leads to the streamlines receding from the stagnation point, and expanding the dissipation pattern away from it.

By the end of the cycle at $\xi = \xi_4$, the total energy transfer from the waves to the rolls, $\langle \mathcal{T}_{w\to r} \rangle_\Omega$, is halfway to its maximum value (see figure 8(d)), and its distribution starts resembling that observed at time ξ_1 (see figure 10(d)). This reflects the fact that the destruction of the old streak is underway by time ξ_4, and waves are already being produced.

4.3. *Waves*

To complete the description of the PSSP, the distribution of the wave energy density $\hat{\mathcal{E}}$, the transfer from the streaks to the waves, $\mathcal{T}_{s\to w}$, and the wave dissipation $\mathcal{D}_w$ must be explored. At high Reynolds number, wave energy, and its transfer terms, are expected to concentrate along lines of constant total streamwise velocity, $U + \mathcal{U} = c$, where c is the (real) phase speed of the waves (so-called critical layers). Figure 12 shows the wave energy components $\hat{\mathcal{E}}$, $\mathcal{T}_{s\to w}$, $\mathcal{T}_{w\to r}$ and $\mathcal{D}_w$ at the same times t_1 to t_4 along with contour lines of constant total streamwise velocity (critical layer candidates). The timing and spatial distribution of the wave energy and its transfer terms agree with the dynamics deduced when analysing the rolls. In particular, the wave energy $\hat{\mathcal{E}}$ is high during the streak destruction period of the cycle (figure 12(a,d)), and the energy concentrates around the stagnation point where this destruction occurs. As expected, the wave dissipation $\mathcal{D}_w$ is also high during these periods and overlaps spatially with the wave energy. A closer inspection of figures 12 (c,d) indicates that, in the lead-up to the streak destruction, the wave energy concentrates in the region between the upper part of the streak and the stagnation point. This indicates that the streak begins to lose stability (to waves) before it completely overlaps with the region of largest strain rate.

Since the laminar flow decays exponentially away from the wall ($|U| \leqslant 0.1$ for $y \gtrsim 1.3$), but the streaks are $O(1)$ before they dissipate, contours of total streamwise velocity $U + \mathcal{U}$ in the vicinity of the streak are strongly shaped by the streak velocity $\mathcal{U}$ and are similar to contours of the streak velocity alone for $y \gtrsim 2$. During the middle part of the cycle, when the streak is rising from its initial position towards the stagnation point (figure 12(b,c)) this results in open contours of $U + \mathcal{U}$ bending up and around the streak. However, at the end of the cycle (and beginning of the next cycle), a region of closed contours forms around the stagnation point (figures 12(d,a)). The waves are most active during this time, and so they become 'trapped' in this region by the closed total streamwise velocity contours. This trapping causes the transfer to the rolls, $\mathcal{T}_{w\to r}$, to be focused around the stagnation point.

Figure 13 shows the two transfer terms, $\mathcal{T}_{s\to w}$ and $\mathcal{T}_{w\to r}$, in more detail around the stagnation point when the waves are most active at time t_1. The transfer from the waves to the rolls, $\mathcal{T}_{w\to r}$, is focused around the contour $c = -0.075$, and so the waves are essentially stationary during the relatively short time that they are active, since they would otherwise take a time $L_x/c \approx 110$ to traverse the streamwise length of the domain. Figure 8(d) shows that $\mathcal{T}_{s\to w}$ and $\mathcal{T}_{w\to r}$ are in phase, so that the energy transfer from streak to waves and then from waves to rolls takes place almost simultaneously within this closed contour region. However, figure 13 shows that the spatial distribution of the two terms is different; transfer to the waves ($\mathcal{T}_{s\to w}$) is centred in a region just below the stagnation point, but transfer to the rolls ($\mathcal{T}_{w\to r}$) ejects fluid horizontally away from the stagnation point, as discussed above.

To complete the picture of the wave dynamics, figure 13 also plots vertical profiles at

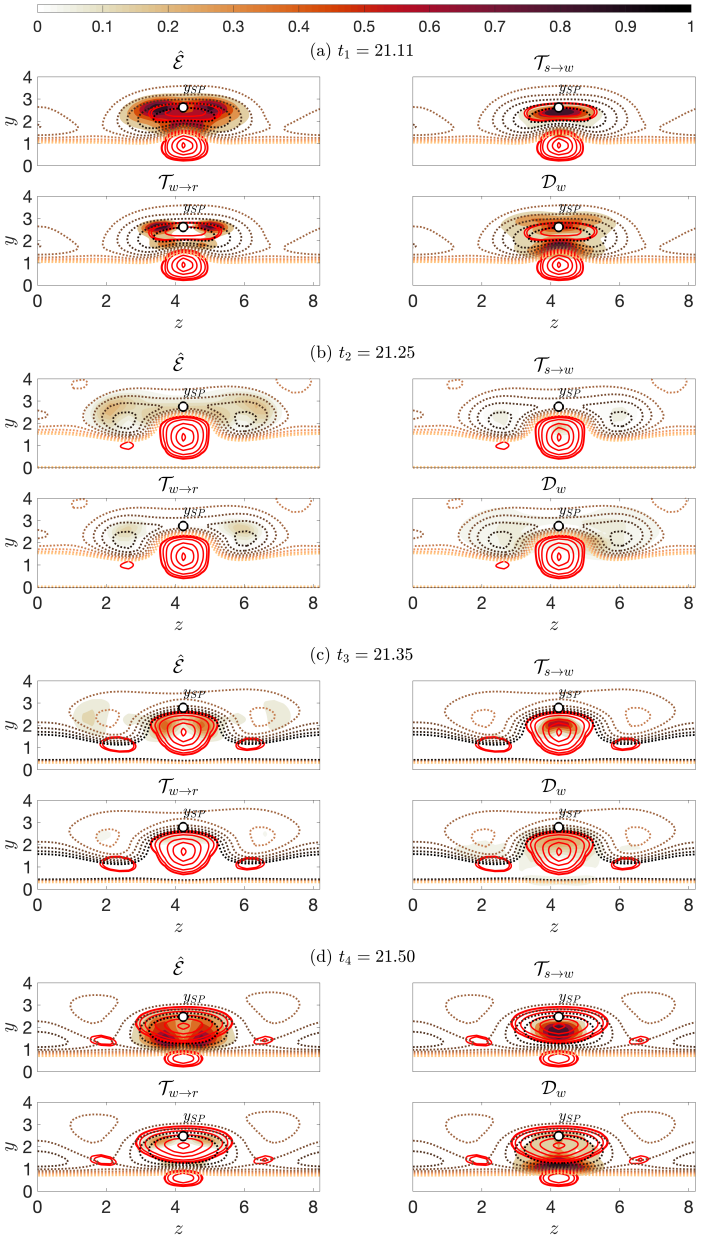

Figure 12: Distribution in the y–z plane of the energy transfer components $\mathcal{T}_{s\to w}$, $\mathcal{T}_{w\to r}$, $\hat{\mathcal{E}}$, and $\mathcal{D}_w$ at times t_1 to t_4, normalised by each of their maximum values across the time window $t_1 \leqslant t \leqslant t_4$. Red contour lines show high streak energy ($\mathcal{E}_s \geqslant 0.25 \max_\Omega\{\mathcal{E}_s\}$). Dotted lines ranging from orange to brown are contour lines of total streamwise velocity $U + \mathcal{U} = c$ for $-0.1 \leqslant c \leqslant 0.1$. The stagnation point is indicated with a circle marker.

three spanwise (z) locations (through the stagnation point, z_C, to its left, z_L, and to its right, z_R) of the streak and roll velocities, along with wave Reynolds stress divergence terms. Figure 13(a) shows that, in the centre of the streak, high streak velocity combines with the spanwise gradient of the spanwise-streamwise wave Reynolds stress ($\partial\langle\hat{u}\hat{w}\rangle/\partial z$) to control

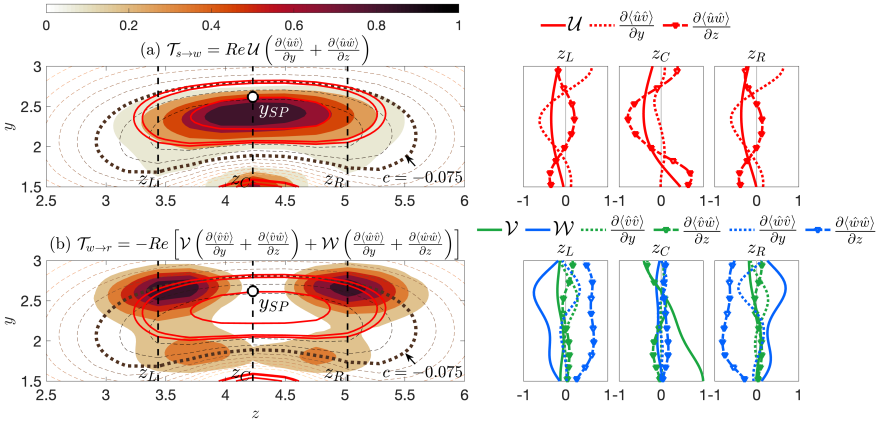

Figure 13: Left: a reproduction of figure 12(a) at $t = t_1$ of (a) $\mathcal{T}_{s\to w}$ and (b) $\mathcal{T}_{w\to r}$ in more detail around the stagnation point. The thicker dotted line corresponds $c = -0.075$. Right: vertical profiles of the streak, roll, and wave Reynolds stress terms that contribute to the energy transfer terms at the three spanwise locations z_L, z_C, and z_R shown on the left.

the energy transfer from streaks to waves, $\mathcal{T}_{s\to w}$ (see the profiles for $z = z_C$). Physically, this represents waves extracting streamwise momentum from the streaks and redistributing it into spanwise wave momentum. The profiles observed at $z = z_L$ and $z = z_R$ in figure 13(b) show that the spanwise roll velocity $\mathcal{W}$ combines with the spanwise gradient of the spanwise-spanwise wave Reynolds stress ($\partial\langle\hat{w}\hat{w}\rangle/\partial z$) to control $\mathcal{T}_{w\to r}$. This represents waves depositing spanwise momentum back into the mean flow (in this case, the rolls). In particular, although the streak velocity $\mathcal{U}$ changes sign every half-period and the symmetries of the (linearised) wave equations ensure that $\langle\hat{u}\hat{w}\rangle$ changes sign also, the fact that the transfer from waves to rolls, $\mathcal{T}_{w\to r}$, is dominated by the sign-definite term $\langle\hat{w}\hat{w}\rangle$ means that the roll velocity $\mathcal{W}$ does not change sign, and by extension neither does $\mathcal{V}$ due to continuity, resulting in the rolls maintaining their flow direction instead of reversing every half-period. This description helps to clarify how the waves mediate the transfer of energy from the streaks to the rolls, allowing the latter to persist and drive the cycle via the lift-up mechanism.

4.4. *Wall stresses*

The PSSP dynamics described above have an effect on the shear stresses $\langle\tau\rangle_{x,z}$ exerted on the wall by the flow. Figure 14(a) plots time series of the average laminar, streak, and roll shear stress at $y = 0$, showing that these three components of the total shear stress are separated by four orders of magnitude, with the laminar shear stress being larger than the streak shear stress, which is in turn larger than the roll shear stress. The streak shear stress is almost periodic, alternating between positive and negative values with a period of T and a phase-shift of approximately $T/2$ with respect to the laminar shear stress. The roll shear stress is irregular and remains negative for most of the time window.

A closer inspection of the phase-shift between the laminar and streak-induced shear stresses in figure 14(a) reveals two types of motion within the edge dynamics. During $20 \lesssim t \lesssim 22$ and $23 \lesssim t \lesssim 25$, the phase-shift between the two shear stresses is close to $T/2$. At the other times in the figure, the streak-induced shear stress shifts slightly earlier by around $T/8$ and changes shape; rather than being nearly symmetric around each local peak value, the peaks become skewed to earlier times. Two such features, at $t \approx 22.5$ and $t \approx 25.5$ correspond to jumps of the structure by $L_z/2$. However, the period $26 \lesssim t \lesssim 30$ contains no such jumps and yet contains the same shear stress pattern. This period is associated with slightly elevated

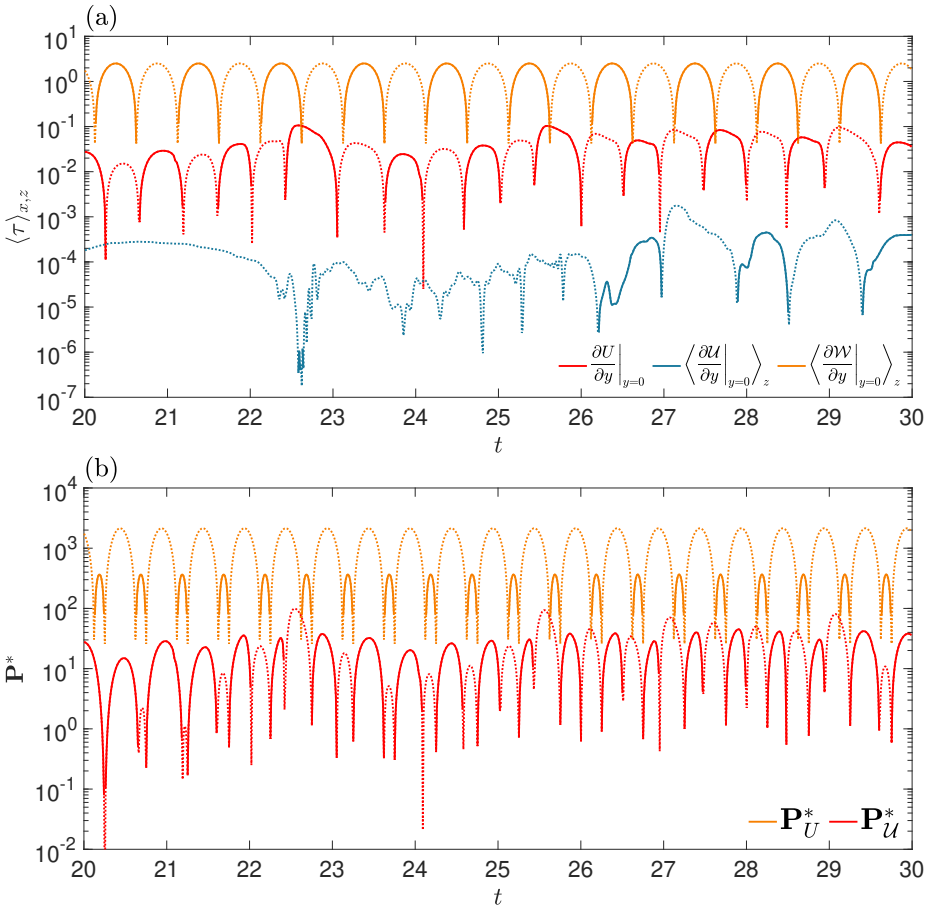

Figure 14: (a) Average shear stress $\langle\tau\rangle_{x,z}$ at the wall due to the laminar (orange), streak (red), and roll (teal) flows for $20 < t < 30$. Dashed lines indicate negative values. (b) Power of energy transfer from the plate to the fluid due to the laminar (orange) and streak (red) flows. Dashed, negative values indicate that the plate is transferring energy to the fluid.

total perturbation energy (c.f. figures 3(a), 5(g,h)) and streak and wave energies (c.f. figure 8(a) and the supplementary movie). The effect of this $T/8$ shift during this more energetic period, though small, is slightly delayed total shear stress peaks, along with slightly elevated shear stresses leading up to and during the laminar shear stress reversals. Within transitional turbulence, which is significantly more energetic than these edge dynamics, Ozdemir *et al.* (2014) observe more exaggerated versions of these two features when $Re \approx 1063$. This suggests that the dynamics presented herein may relate directly to some key processes of transitional turbulence, though future detailed investigation of this hypothesis is necessary.

To analyse the influence of PSSP on the energy input needed to maintain the plate oscillation, figure 14(b) shows the non-dimensional power per unit area of the laminar

and perturbation velocity fields at $y = 0$. These powers are given by

$$\frac{\boldsymbol{P}_U}{\rho\nu U_0} \equiv \boldsymbol{P}^*_U = \left\langle Re\, U \left.\frac{\partial U}{\partial y}\right|_{y=0} \right\rangle_{x,z} \equiv Re\, U \frac{\partial U}{\partial y}, \tag{4.12}$$

$$\frac{\boldsymbol{P}_{\mathcal{U}}}{\rho\nu U_0} \equiv \boldsymbol{P}^*_{\mathcal{U}} = \left\langle Re\, U \left.\frac{\partial u}{\partial y}\right|_{y=0} \right\rangle_{x,z} \equiv \left\langle Re\, U \left.\frac{\partial \mathcal{U}}{\partial y}\right|_{y=0} \right\rangle_{z}, \tag{4.13}$$

where $\boldsymbol{P}_U$ and $\boldsymbol{P}_{\mathcal{U}}$ are the dimensional power associated with the laminar and the perturbation streak flows respectively. The figure shows that both the laminar and the streak powers are periodic with a period of $T/2$. Similarly to their shear stresses, the laminar and streak power are out of phase with each other.

Figure 14(b) also shows that positive and negative power values are different in magnitude; the laminar power has larger negative peaks than positive peaks and so is a net consumer of energy, whereas the streak power has larger positive peaks than negative peaks and so is a net contributor of energy to the plate motion. The back-and-forth motion of the plate must overcome the inertia of the fluid in order to repeatedly reverse its direction, and so the average energy transfer over each cycle must be from the plate to the fluid. However, there are periods within each cycle during which energy is instantaneously transferred back to the plate, as the inertia of the fluid drives the plate in the same direction as it travels. These windows are short; the laminar flow shear force F_{τ_ℓ} is in the same direction as the plate velocity U for $1/8 < \xi < 1/4$ and $5/8 < \xi < 3/4$ (for a total of $1/4$ of the whole cycle), as shown in figure 15. Furthermore, the power of energy transfer from the laminar flow back to the plate is substantially smaller than during the rest of the cycle when the laminar flow gains energy from the plate. On the other hand, the perturbation streak flow is a net contributor to the plate energy (albeit at a substantially lower power), reducing the total energy consumption. The relative timing during the cycle means that the streak inertia contributes most to reducing the power transfer from the plate when the laminar shear force is most strongly opposed to the plate motion.

5. Conclusions

In this work, we characterised and analysed the flow structures of an edge state in the oscillatory Stokes boundary layer. We used DNS to perform edge tracking of the manifold that separates flow trajectories which either re-laminarise or become turbulent. The edge was tracked for approximately 40 diffusive time units for $Re = 1000$. The edge dynamics are organised into streak-like structures of size $O(1)$, which originate a little above the oscillating wall and migrate upward at a speed of $2\sqrt{\pi}$ (the phase speed of travelling features of the laminar flow), dissipating around $y \lesssim 3$. This behaviour is repeated cyclically (twice within each wall-oscillation cycle), and results in alternating production- and dissipation-dominated phases within each period. The formation and upward motion of the structures occurs predominantly during the wall deceleration phase, and their loss of coherence and eventual dissipation near $y \lesssim 3$ occurs during the acceleration phase. These structures are isolated in the spanwise direction for much of the edge state trajectory, sporadically duplicating and occupying the entire spanwise extent of the flow domain before a new spanwise localised state emerges. We focussed on the localised flow periods in order to understand and describe the dynamics of the edge.

We performed a streak-roll-wave (SRW) decomposition of the velocity field in order to interpret the cycle using flow components which comprise the well-known Self Sustaining Process (SSP) (Hall & Smith 1991; Waleffe 1997), and in doing so detailed a periodic,

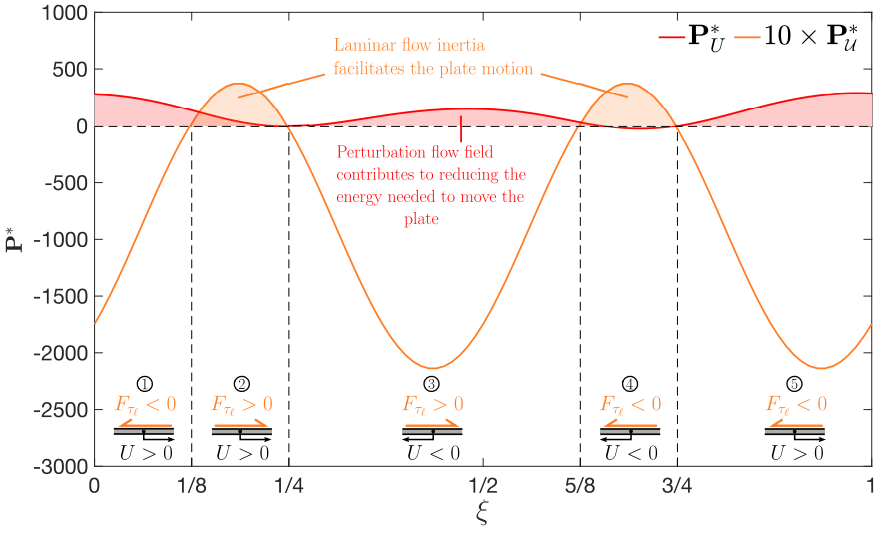

Figure 15: Power of energy transfer transfer from the plate to the fluid for $20 < t < 21$ (indicated by $0 < \xi < 1$ with $k = 20$) for the laminar (yellow) and streak (red) flows. Negative values indicate energy transfer from the plate to fluid. In the bottom of the plot, the sketches show the direction of the plate velocity and the laminar shear force exerted on the plate.

spatially evolving version of the typically steady or confined SSP. The rolls are composed of four counter-rotating recirculation cells of diameter $\approx L_z/2$ that converge into a stagnation point at a height $y_{SP} \lesssim 3$. The rolls are persistent, only slightly modifying their shape over the cycle, and this relatively unchanging flow component allows for the so-called Periodic Self Sustaining Process (PSSP) to be generated.

The stages of the cycle can be summarised as follows: (i) at the beginning of the cycle, the rolls lift high-velocity fluid near the oscillating wall upward to create a large velocity defect, creating and sustaining the streaks, (ii) once a streak has formed, it can only continue to grow and exist within a region having the same sign of laminar shear as when it was created, and regions of constant laminar shear sign migrate upward at a speed of $2\sqrt{\pi}$, thus controlling the upward migration of the streaks, (iii) the upward moving streaks eventually reach the stagnation point at $y_{SP} \lesssim 3$ and cannot be transported any further owing to a reversal in the sign of the streak production rate, and are instead torn apart by the stagnation point, dissipating while transferring a small amount of energy to the waves, (iv) lines of constant total streamwise velocity (potential critical layers) trap the waves in the vicinity of the stagnation point, and the waves transfer a small amount of energy to the rolls via a Reynolds stress directed in the spanwise direction away from the stagnation point, (v) mass conservation within the roll system ensures that the upwards roll velocity where the streaks are created maintains its energy against dissipation, thus sustaining the cycle by creating a new (oppositely signed) streak. The dynamics of the edge at $Re = 1200$ are quantitively similar to those at $Re = 1000$, although no clear scaling between the two Reynolds numbers was observed, due to their modest size and small separation. Additionally, edge dynamics in a narrower domain at $Re = 1000$ were somewhat chaotic due to their confinement, although qualitatively similar structures were observed.

Finally, a brief analysis of the effect of the edge dynamics on the wall shear stress and power consumption was performed. The shear stress exerted by the streaks contributes (slightly) to

reducing the energy needed to move the plate, and this effect occurs when the laminar flow is extracting energy from the plate with the most power.

The PSSP unveils a fundamental mechanism by which streaks may be raised away from the laminar boundary layer, growing during the deceleration phase and with a phase-lag to the laminar flow. Were this process to occur at a slightly larger amplitude away from the edge state, then presumably adjacent streaks would readily combine into hairpin vortices and deliver spanwise ejections into the free stream which break down to turbulence, as in the observed bypass transition process. This work therefore provides evidence towards a key component of bypass transition, that of streak growth and regeneration, being fundamentally tied to physics within the boundary layer itself and its self-contained interaction with the background laminar flow. Confirmation of this would require an analysis of the linear stability properties of the edge trajectory, or the computation of its optimally growing disturbances (see, e.g. Andersson *et al.* 1999; Luchini 2000; Cherubini & De Palma 2015; Firano *et al.* 2015). A careful analysis of such disturbances for this fully three-dimensional, time-varying edge trajectory represents a significant future endeavour. We also note that the streaks presented here bear some resemblance to those found in other oscillating shear flows, particularly large laminar separation bubbles (Gaster 1966; Pauley *et al.* 1990) and structures associated with their slow mode of oscillation (Cherubini *et al.* 2010*a*,*b*; Rodríguez *et al.* 2021; Verdoya *et al.* 2021; Malmir *et al.* 2024). However, a direct comparison between these objects is not easily made within the current work.

It remains to be seen how the structures in the PSSP scale with Re and to what extent the structures in fully-developed Stokes-layer turbulence resemble the edge state PSSP described herein. Repeated, extensive attempts were made to converge dynamics on the edge to a periodic orbit using a Newton–GMRES–hookstep solver but to no avail, potentially suggesting that any coherent edge state structures are quasi-periodic. Though computationally expensive, a fully localised edge trajectory in a large domain should be sought. Not only would such a structure be most physically relevant, it may also represent truly periodic behaviour if the quasiperiodicity of the results presented here owe their origin to interactions between neighbouring streaks through the periodic boundaries. Nevertheless, the current identification and full description of periodic self-sustaining motion within the oscillating Stokes boundary layer sets the groundwork for interpreting its structural dynamics alongside better studied steady or confined shear flows.

Supplementary data. A movie accompanying figure 6 is available.

Acknowledgements. Dr Dan Lucas is thanked for several insightful conversations about the usage of his Newton–GMRES–hookstep solver. Three anonymous reviewers are thanked for their comments and contributions towards the improvement of the manuscript.

Funding. This research was funded by an EPSRC New Investigator Award (EP/W021099/1).

Declaration of interests. The authors report no conflict of interest.

Data availability statement. The initial condition and grid file used for edge tracking are available at https://doi.org/10.15132/10000267. The edge tracking extension of Diablo is available at https://github.com/jsandoval001/Diablo_edge_tracking.

Author ORCIDs. J. Sandoval, https://orcid.org/0000-0002-6483-4237; T. Eaves, https://orcid.org/0000-0003-3473-1306

Author contributions. Both authors contributed to all aspects of the manuscript.

Appendix A. Energetics of the SRW decomposition

Projecting the streak equation (4.2) onto the streak velocity field $\mathcal{U}$, we obtain

$$\frac{\partial \mathcal{E}_s}{\partial t} + Re\mathcal{U}_j \frac{\partial \mathcal{E}_s}{\partial x_j} = -Re\left(\mathcal{U}\mathcal{V}\frac{\partial U}{\partial y} + \mathcal{U}\frac{\partial \left\langle \hat{u}\hat{u}_j \right\rangle_x}{\partial x_j}\right) + \frac{\partial^2 \mathcal{E}_s}{\partial x_j \partial x_j} - \frac{\partial \mathcal{U}}{\partial x_j}\frac{\partial \mathcal{U}}{\partial x_j}, \tag{A 1}$$

where $\mathcal{E}_s = \frac{1}{2}\mathcal{U}^2$ is the streak energy density. Projecting (4.3) onto $\mathcal{V}$ and (4.4) onto $\mathcal{W}$, summing the resulting equations, we obtain

$$\begin{aligned}\frac{\partial \mathcal{E}_r}{\partial t} + Re\mathcal{U}_j \frac{\partial \mathcal{E}_r}{\partial x_j} = &-\frac{\partial \left(\mathcal{U}_j \mathscr{P}\right)}{\partial x_j} - Re\left(\mathcal{V}\frac{\partial \left\langle \hat{v}\hat{u}_j \right\rangle_x}{\partial x_j} + \mathcal{W}\frac{\partial \left\langle \hat{w}\hat{u}_j \right\rangle_x}{\partial x_j}\right) \\ &+ \frac{\partial^2 \mathcal{E}_r}{\partial x_j \partial x_j} - \frac{\partial \mathcal{V}}{\partial x_j}\frac{\partial \mathcal{V}}{\partial x_j} - \frac{\partial \mathcal{W}}{\partial x_j}\frac{\partial \mathcal{W}}{\partial x_j},\end{aligned} \tag{A 2}$$

where $\mathcal{E}_r = \frac{1}{2}(\mathcal{V}^2 + \mathcal{W}^2)$ is the roll energy density.

By construction, $\mathcal{E} = \mathcal{E}_s + \mathcal{E}_r + \hat{\mathcal{E}}$, where $\mathcal{E} = \langle e \rangle_x$ is the x-averaged total energy density and $\hat{\mathcal{E}} = \langle \frac{1}{2}|\hat{\boldsymbol{u}}|^2 \rangle_x$ is the x-averaged wave energy density, given that the cross-term $\langle \boldsymbol{\mathcal{U}} \cdot \hat{\boldsymbol{u}} \rangle_x$ in $\mathcal{E}$ vanishes since $\boldsymbol{\mathcal{U}}$ does not depend on x and $\langle \hat{\boldsymbol{u}} \rangle_x = 0$. Therefore, the equation for the waves kinetic energy $\hat{\mathcal{E}}$ can be obtained from $\frac{\partial \hat{\mathcal{E}}}{\partial t} = \frac{\partial \mathcal{E}}{\partial t} - \frac{\partial \mathcal{E}_s}{\partial t} - \frac{\partial \mathcal{E}_r}{\partial t}$, which leads to

$$\begin{aligned}\frac{\partial \hat{\mathcal{E}}}{\partial t} + Re\mathcal{U}_j \frac{\partial \hat{\mathcal{E}}}{\partial x_j} = &-\frac{\partial \langle \hat{u}_j \hat{p} \rangle_x}{\partial x_j} - Re\left[\langle \hat{u}\hat{v} \rangle_x \frac{\partial U}{\partial y} + \langle \hat{u}_i \hat{u}_j \rangle_x \frac{\partial \mathcal{U}_i}{\partial x_j} + \left\langle \hat{u}_i \frac{\partial (\hat{u}_i \hat{u}_j)}{\partial x_j} \right\rangle_x\right] \\ &+ \frac{\partial^2 \hat{\mathcal{E}}}{\partial x_j \partial x_j} - \left\langle \frac{\partial \hat{u}_i}{\partial x_j}\frac{\partial \hat{u}_i}{\partial x_j} \right\rangle_x.\end{aligned} \tag{A 3}$$

Integrating these equations over the whole domain gives evolution equations for the total streak $E_s \equiv \langle \mathcal{E}_s \rangle_\Omega$, roll $E_r \equiv \langle \mathcal{E}_r \rangle_\Omega$, and wave $\hat{E} \equiv \langle \hat{\mathcal{E}} \rangle_\Omega$ energies, and defines production ($\mathcal{P}$), transfer ($\mathcal{T}$), and dissipation ($\mathcal{D}$) rates associated with the laminar (ℓ), streak (s), roll

(*r*), and wave (*w*) components of the flow:

$$\frac{\mathrm{d}E_s}{\mathrm{d}t} = \left\langle \underbrace{-Re\,\mathcal{U}\mathcal{V}\frac{\partial U}{\partial y}}_{\mathcal{P}_{\ell\to s}} \right\rangle_\Omega - \left\langle \underbrace{Re\,\mathcal{U}\left(\frac{\partial\langle\hat{u}\hat{v}\rangle}{\partial y} + \frac{\partial\langle\hat{u}\hat{w}\rangle}{\partial z}\right)}_{\mathcal{T}_{s\to w}} \right\rangle_\Omega - \left\langle \underbrace{\left(\frac{\partial\mathcal{U}}{\partial y}\right)^2 + \left(\frac{\partial\mathcal{U}}{\partial z}\right)^2}_{\mathcal{D}_s} \right\rangle_\Omega \tag{A 4}$$

$$\frac{\mathrm{d}E_r}{\mathrm{d}t} = \left\langle \underbrace{-Re\left[\mathcal{V}\left(\frac{\partial\langle\hat{v}\hat{v}\rangle}{\partial y} + \frac{\partial\langle\hat{v}\hat{w}\rangle}{\partial z}\right) + \mathcal{W}\left(\frac{\partial\langle\hat{w}\hat{v}\rangle}{\partial y} + \frac{\partial\langle\hat{w}\hat{w}\rangle}{\partial z}\right)\right]}_{\mathcal{T}_{w\to r}} \right\rangle_\Omega$$

$$- \left\langle \underbrace{\left(\frac{\partial\mathcal{V}}{\partial y}\right)^2 + \left(\frac{\partial\mathcal{V}}{\partial z}\right)^2 + \left(\frac{\partial\mathcal{W}}{\partial y}\right)^2 + \left(\frac{\partial\mathcal{W}}{\partial z}\right)^2}_{\mathcal{D}_r} \right\rangle_\Omega, \tag{A 5}$$

$$\frac{\mathrm{d}\hat{E}}{\mathrm{d}t} = \left\langle \underbrace{-Re\,\hat{u}\hat{v}\frac{\partial U}{\partial y}}_{\mathcal{P}_{\ell\to w}} \right\rangle_\Omega + \left\langle \underbrace{Re\,\mathcal{U}\left(\frac{\partial\langle\hat{u}\hat{v}\rangle}{\partial y} + \frac{\partial\langle\hat{u}\hat{w}\rangle}{\partial z}\right)}_{\mathcal{T}_{s\to w}} \right\rangle_\Omega$$

$$- \left\langle \underbrace{-Re\left[\mathcal{V}\left(\frac{\partial\langle\hat{v}\hat{v}\rangle}{\partial y} + \frac{\partial\langle\hat{v}\hat{w}\rangle}{\partial z}\right) + \mathcal{W}\left(\frac{\partial\langle\hat{w}\hat{v}\rangle}{\partial y} + \frac{\partial\langle\hat{w}\hat{w}\rangle}{\partial z}\right)\right]}_{\mathcal{T}_{w\to r}} \right\rangle_\Omega - \left\langle \underbrace{\frac{\partial\hat{u}_i}{\partial x_j}\frac{\partial\hat{u}_i}{\partial x_j}}_{\mathcal{D}_w} \right\rangle_\Omega. \tag{A 6}$$

REFERENCES

Adcock, T.A.A., Draper, S., Willden, R.H.J. & Vogel, C.R. 2021 The fluid mechanics of tidal stream energy conversion. *Annu. Rev. Fluid Mech.* **53** (1), 287–310.

Andersson, P., Berggren, M. & Henningson, D. S. 1999 Optimal disturbances and bypass transition in boundary layers. *Phys. Fluids* **11**, 134–150.

Biau, D. 2016 Transient growth of perturbations in stokes oscillatory flows. *J. Fluid Mech.* **794**, R4.

Blennerhassett, P.J. & Bassom, A.P. 2002 The linear stability of flat Stokes layers. *J. Fluid Mech.* **464**, 393–410.

Blennerhassett, P.J. & Bassom, A.P. 2008 On the linear stability of Stokes layers. *Phil. Trans. R. Soc. A* **366** (1876), 2685–2697.

Blondeaux, P., Pralits, J.O. & Vittori, G. 2021 On the stability of the boundary layer at the bottom of propagating surface waves. *J. Fluid Mech.* **928**, A26.

Blondeaux, P. & Vittori, G. 2021 Revisiting the momentary stability analysis of the stokes boundary layer. *J. Fluid Mech.* **919**, A36.

Budanur, N.B., Short, K.Y., Farazmand, M., Willis, A.P. & Cvitanović, P. 2017 Relative periodic orbits form the backbone of turbulent pipe flow. *J. Fluid Mech.* **833**, 274–301.

Butler, K.M. & Farrell, B.F. 1992 Three-dimensional optimal perturbations in viscous shear flow. *Phys. Fluids A* **4**, 1637–1650.

Cherubini, S. & De Palma, P. 2015 Minimal-energy perturbations rapidly approaching the edge state in Couette flow. *J. Fluid Mech.* **764**, 572–598.

Cherubini, S., Robinet, J.-Ch. & De Palma, P. 2010*a* The effects on non-normality and nonlinearity of the Navier–Stokes operator on the dynamics of a large laminar separation bubble. *Phys. Fluids* **22**, 014102.

Cherubini, S., Robinet, J.-Ch., De Palma, P. & Alizard, F. 2010*b* The onset of three-dimensional centrifugal global modes and their nonlinear development in a recirculating flow over a flat surface. *Phys. Fluids* **22**, 114102.

Costamagna, P., Vittori, G. & Blondeaux, P. 2003 Coherent structures in oscillatory boundary layers. *J. Fluid Mech.* **474**, 1–33.

Duguet, Y., Schlatter, P. & Henningson, D.S. 2009 Localized edge states in plane couette flow. *Phys. Fluids* **21** (11), 111701.

Eaves, T.S. & Caulfield, C.P. 2015 Disruption of SSP/VWI states by a stable stratification. *J. Fluid Mech.* **784**, 548–564.

Ebadi, A., White, C.M., Pond, I. & Dubief, Y. 2019 Mean dynamics and transition to turbulence in oscillatory channel flow. *J. Fluid Mech.* **880**, 864–889.

Firano, M., Cherubini, S., Robinet, J.-Ch. & De Palma, P. 2015 Hairpin-like optimal perturbations in plane Poiseuille flow. *J. Fluid Mech.* **775**, R1.

Fytanidis, D.K., García, M.H. & Fischer, P.F. 2021 Mean flow structure and velocity–bed shear stress maxima phase difference in smooth wall, transitionally turbulent oscillatory boundary layers: direct numerical simulations. *J. Fluid Mech.* **928**, A33.

Gaster, M. 1966 The structure and behaviour of laminar separation bubbles. *AGARD* **CP-4**, 813–854.

Gatti, D. & Quadrio, M. 2016 Reynolds-number dependence of turbulent skin-friction drag reduction induced by spanwise forcing. *J. Fluid Mech.* **802**, 553–582.

Gong, M., Xiong, C., Mao, X., Cheng, L., Wang, S.-P. & Zhang, A.-M. 2022 Non-modal growth of finite-amplitude disturbances in oscillatiory boundary layer. *J. Fluid Mech.* **943**, A45.

Hall, P. & Sherwin, S. 2010 Streamwise vortices in shear flows: harbingers of transition and the skeleton of coherent structures. *J. Fluid Mech.* **661**, 178–205.

Hall, P. & Smith, F.T. 1991 On strongly nonlinear vortex/wave interactions in boundary-layer transition. *J. Fluid Mech.* **227**, 641–666.

Jensen, B.L., Sumer, B.M. & Fredsøe, J. 1989 Turbulent oscillatory boundary layers at high reynolds numbers. *J. Fluid Mech.* **206**, 265–297.

Kawahara, G., Uhlmann, M. & van Veen, L. 2012 The significance of simple invariant solutions in turbulent flows. *Annu. Rev. Fluid Mech.* **44**, 203–225.

von Kerczek, C. & Davis, S. H. 1974 Linear stability theory of oscillatory Stokes layers. *J. Fluid Mech.* **62**, 753–773.

Kerswell, R. R. 2018 Nonlinear nonmodal stabilith theory. *Annu. Rev. Fluid Mech.* **50**, 319–345.

Khapko, T., Kreilos, T., Schlatter, P., Duguet, Y., Eckhardt, B. & Henningson, D.S. 2013 Localized edge states in the asymptotic suction boundary layer. *J. Fluid Mech.* **717**, R6.

Khapko, T., Kreilos, T., Schlatter, P., Duguet, Y., Eckhardt, B. & Henningson, D.S. 2016 Edge states as mediators of bypass transition in boundary-layer flows. *J. Fluid Mech.* **801**, R2.

Kim, L. & Moehlis, J. 2008 Characterizing the edge of chaos for a shear flow model. *Phys. Rev. E* **78** (3), 036315.

Kreilos, T., Veble, G., Schneider, T.M. & Eckhardt, B. 2013 Edge states for the turbulence transition in the asymptotic suction boundary layer. *J. Fluid Mech.* **726**, 100–122.

Ku, D.N. 1997 Blood flow in arteries. *Annu. Rev. Fluid Mech.* **29** (1), 399–434.

Landahl, M.T. 1980 A note on an algebraic instabililty of inviscid parallel shear flows. *J. Fluid Mech.* **98**, 243–251.

Linot, A.J., Schmid, P.J. & Taira, K. 2024 On the laminar solutions and stability of accelerating and decelerating channel flows. *J. Fluid Mech.* **999**, A43.

Luchini, P. 2000 Reynolds-number-independent instability of the boundary layer over a flat surface: optimal perturbations. *J. Fluid Mech.* **404**, 289–309.

Luo, J. & Wu, X. 2010 On the linear instability of a finite stokes layer: instantaneous versus floquet modes. *Phys. Fluids* **22** (5), 054104.

Malmir, F., Di Labbio, G., Le Floc'h, A., Dufresne, L, Weiss, J. & Vétel, J. 2024 Low-frequency unsteadiness in laminar separation bubbles. *J. Fluid Mech.* **999**, A99.

Mier, J.M., Fytanidis, D.K. & García, M.H. 2021 Mean flow structure and velocity–bed shear stress maxima phase difference in smooth wall, transitionally turbulent oscillatory boundary layers: experimental observations. *J. Fluid Mech.* **922**, A29.

Mujal-Colilles, A., Christensen, K.T., Bateman, A. & Garcia, M.H. 2016 Coherent structures in oscillatory flows within the laminar-to-turbulent transition regime for smooth and rough walls. *J. Hydraulic Res.* **54**, 502–515.

Orr, W. M'F. 1907 The stability or instability of the steady motions of a perfect liquid and of a viscous liquid. Part I: A perfect liquid. *Proc. R. Irish Acad. Sect. A* **27**, 9–68.

Ozdemir, C.E., Hsu, T.-J. & Balachandar, S. 2014 Direct numerical simulations of transition and turbulence in smooth-walled stokes boundary layer. *Phys. Fluids* **26** (4), 041403.

Pauley, L. L., Moin, P. & Reynolds, W. C. 1990 The structure of two-dimensional separation. *J. Fluid Mech.* **220**, 397–411.

Pier, B. & Schmid, P.J. 2017 Linear and nonlinear dynamics of pulsatile channel flow. *J. Fluid Mech.* **815**, 435–480.

Pier, B. & Schmid, P.J. 2021 Optimal energy growth in pulsatile channel and pipe flows. *J. Fluid Mech.* **926**, A11.

Pretty, A., Davies, C. & Thomas, C. 2021 Onset of absolutely unstable behaviour in the stokes layer: a Floquet approach to the Briggs method. *J. Fluid Mech.* **928**, A23.

Ramage, A., Davies, C., Thomas, C. & Togneri, M. 2020 Numerical simulation of the spatio-temporal development of linear disturbances in Stokes layers: absolute instability and the effects of high frequency harmonics. *Phys. Rev. Fluids* **5**, 103901.

Rodríguez, D., Gennaro, E. M. & Souza, L. F. 2021 Self-excited primary and secondary instability of laminar separation bubbles. *J. Fluid Mech.* **906**, A13.

Sarpkaya, T. 1993 Coherent structures in oscillatory boundary layers. *J. Fluid Mech.* **253**, 105–140.

Schneider, T.M. & Eckhardt, B. 2006 Edge of chaos in pipe flow. *Chaos* **16** (4), 041102.

Schneider, T.M., Eckhardt, B. & Yorke, J.A. 2007 Turbulence transition and the edge of chaos in pipe flow. *Phys. Rev. Lett.* **99** (3), 034502.

Schneider, T.M., Marinc, D. & Eckhardt, B. 2010 Localized edge states nucleate turbulence in extended plane couette cells. *J. Fluid Mech.* **646**, 441–451.

Skufca, J.D., Yorke, J.A. & Eckhardt, B. 2006 Edge of chaos in a parallel shear flow. *Phys. Rev. Lett.* **96** (17), 174101.

Spalart, P.R. & Baldwin, B.S. 1987 Direct simulation of a turbulent oscillating boundary layer. *Tech. Rep.*. NASA.

Taylor, C.A. & Draney, M.T. 2004 Experimental and computational methods in cardiovascular fluid mechanics. *Annu. Rev. Fluid Mech.* **36** (1), 197–231.

Taylor, J.R. 2008 *Numerical simulations of the stratified oceanic bottom boundary layer*. PhD thesis, University of California, San Diego.

Toh, S. & Itano, T. 2003 A periodic-like solution in channel flow. *J. Fluid Mech.* **481**, 67–76.

Verdoya, J., Dellacasagrande, M., Lengani, D., Simoni, D. & Ubaldi, M. 2021 Inspection of structures interaction in laminar separation bubbles with extended proper orthogonal decomposition applied to multi-plane particle image velocimetry data. *Phys. Fluids* **33**, 043607.

Waleffe, F. 1997 On a self-sustaining process in shear flows. *Phys. Fluids* **9** (4), 883–900.

Xiong, C., Qi, X., Gao, A., Xu, H., Ren, C. & Cheng, C. 2020 The bypass transition mechanism of the stokes boundary layer in the intermittently turbulent regime. *J. Fluid Mech.* **896**, A4.